

Non-Destructive Evaluation of 3D-Printed Parts Using Algorithm-Aided Infrared Thermography

By

Kailey Nicole Newcome

Thesis

Submitted to the Faculty of the
Graduate School of Vanderbilt University
in partial fulfillment of the requirements

for the degree of

MASTER OF SCIENCE

in

Civil and Environmental Engineering

December 18, 2021

Nashville, Tennessee

Approved:

Douglas Adams, Ph.D.

Ravindra Duddu, Ph.D.

Pranav Karve, Ph.D.

Contents

Chapter 1: Introduction	1
1.1 Overview of Additive Manufacturing (AM).....	1
1.1.1 VAT Photopolymerization.....	2
1.1.2 Material Jetting	3
1.1.3 Binder Jetting	3
1.1.4 Material Extrusion.....	3
1.1.5 Powder Bed Fusion	4
1.1.6 Sheet Lamination	4
1.1.7 Directed Energy Deposition.....	4
1.1.8 Conclusion	5
1.2 Quality Control Methods Employed in Manufacturing	5
1.2.1 Destructive Quality Monitoring	6
1.2.2 Nondestructive Quality Monitoring	6
1.3 Review of Nondestructive Quality Monitoring for AM	6
1.3.1 Visual inspection.....	6
1.3.2 Acoustic Techniques	7
1.3.3 Imaging Techniques.....	8
1.3.4 Optical Techniques	8
Chapter 2: Mathematical Approach	12
2.1 Heat Transfer Equations.....	12
2.2 Use of the Algorithm for Determining Thermal Conductivity	13
Chapter 3: Materials and Methodology	15
3.1 Materials	15
3.1.1 Epoxy	15
3.1.2 Epoxy with Hole	15
3.1.3 3D-printed materials	15
3.2 Methodology	16
3.2.1 Preliminary Experimental Methods	16
3.2.2 Data Collection via the Heat Soak Oven Method	17
3.2.3 Data Processing Methodology	19
Chapter 4: Results	20

4.1	Epoxy	20
4.1.1	Epoxy Test 1	20
4.1.2	Epoxy Test 2	27
4.2	Epoxy with Hole	30
4.2.1	Epoxy Hole Test 1.....	31
4.2.2	Epoxy Hole Test 2.....	34
4.3	3D-Printed Specimens	38
4.3.1	3D-Printed Specimen Test 1	38
4.3.2	3D-Printed Specimen Test 2	40
4.3.3	Discussion on 3D-Printed Specimen Results.....	41
Chapter 5: Conclusion.....		42
References.....		43
Appendices.....		47
Appendix A:.....		47

LIST OF FIGURES

Figure	Page
2. 1: 3D domain (Ω) of specimens used in FTCS model	13
3. 1: Samples used in testing (from left to right: epoxy, epoxy with hole, and ABS)	16
3. 2: Nodal network example	18
3. 3: Schematic of IR camera and specimen experimental set up	19
4. 1: Frequency distribution of Epoxy Test 1.....	21
4. 2: Normal probability paper for Epoxy Test 1	22
4. 3: Lognormal probability paper for Epoxy Test 1	22
4. 4: New frequency distribution of Epoxy Test 1	24
4. 5: Normal probability paper for Epoxy Test 1	24
4. 6: Lognormal probability paper for Epoxy Test 1	25
4. 7: Frequency distribution for each node and its average thermal conductivity for Epoxy Test 1	26
4. 8: Frequency distribution of Epoxy Test 2.....	27
4. 9: Normal probability paper for Epoxy Test 2.....	28
4. 10: Lognormal probability paper for Epoxy Test 2	28
4. 11: Frequency distribution for each node and its average thermal conductivity for Epoxy Test 2.....	30
4. 12: Frequency distribution of Epoxy Hole Test 1	31
4. 13: Normal probability paper for Epoxy Hole Test 1	32
4. 14: Lognormal probability paper for Epoxy Hole Test 1.....	32
4. 15: Frequency distribution for each node and its average thermal conductivity for Epoxy Hole Test 1	34
4. 16: Frequency distribution of Epoxy Hole Test 2.....	35
4. 17: Normal probability paper for Epoxy Hole Test 2	35
4. 18: Lognormal probability paper for Epoxy Hole Test 2.....	36

4. 19: Frequency distribution for each node and its average thermal conductivity for Epoxy Hole Test 2	37
4. 20: Comparison of experimental and synthetic data cooling curved ($k_x = 0.16$ W/mK, $k_y = 0.12$ W/mK, $k_z = 0.04$ W/mK)	39
4. 21: Comparison of experimental and synthetic data cooling curved ($k_x = 0.13$ W/mK, $k_y = 0.12$ W/mK, $k_z = 0.04$ W/mK)	39
4. 22: Comparison of experimental and synthetic data cooling curved ($k_x = 0.16$ W/mK, $k_y = 0.09$ W/mK, $k_z = 0.04$ W/mK)	39
4. 23: Comparison of experimental and synthetic data cooling curved ($k_x = 0.16$ W/mK, $k_y = 0.15$ W/mK, $k_z = 0.04$ W/mK)	40
4. 24: Comparison of experimental and synthetic data cooling curved ($k_x = 0.19$ W/mK, $k_y = 0.12$ W/mK, $k_z = 0.04$ W/mK)	40
4. 25: Schematic of the 3D-Printed Part	41
A.1: Schematic of surface boundaries	48
A.2: Schematic of edge boundaries	49
A.3: Schematic of corner boundaries	50

LIST OF TABLES

Figure	Page
4. 1: Results of chi-square test for Epoxy Test 1	23
4. 2: Results of outlier test	23
4. 3: Results of chi-square test for a Gaussian distribution for Epoxy Test 1 without outliers.....	25
4. 4: Results of chi-square test for a lognormal distribution for Epoxy Test 1 without outliers.....	25
4. 5: Gaussian chi-square test results for Epoxy Test 2	29
4. 6: Lognormal chi-square test results for Epoxy Test 2	29
4. 7: Gaussian chi-square test results for Epoxy Hole Test 1.....	33
4. 8: Lognormal chi-square test results for Epoxy Hole Test 1	33
4. 9: Gaussian chi-square test results for Epoxy Hole Test 2.....	36
4. 10: Lognormal chi-square test results for Epoxy Hole Test 2	36

Chapter 1: Introduction

Additive manufacturing is a rapidly emerging technology in industry. This process has many benefits compared to more traditional modes of manufacturing, in that it enables greater customization, reduced material waste, and cost-effective low volume production. However, issues such as the high prevalence of flaws in 3D-printed parts have prevented additive manufacturing from becoming more mainstream practice.

To detect these flaws, many nondestructive evaluation techniques have been devised. One of these techniques is infrared thermography. To date, many infrared thermography techniques have lacked connections to the physics of heat transfer to make them as successful as they could be. This research is designed to overcome this issue by using heat transfer principles in combination with infrared technology to devise a new nondestructive evaluation method.

This research explores a nondestructive evaluation method using infrared thermography that estimates the thermal conductivity of 3D-printed parts using a Forward-in-Time, Centered-in-Space heat transfer model. To better understand the context of this work, a literature review involving the areas of additive manufacturing and nondestructive evaluation is provided.

1.1 Overview of Additive Manufacturing (AM)

Additive manufacturing (AM) is one of the most rapidly evolving process innovations in manufacturing. In the AM process, a three-dimensional (3D) model is created with computer aided design (CAD). The CAD file is then sent to a 3D printer that creates the design as a 3D object by adding material layer by layer [1].

Compared to the more traditional subtractive manufacturing process, which creates objects by removing material, the AM process adds and fuses together materials to create 3D parts. “3D printing” is often used when referring to additive manufacturing; however, 3D printing is only one step in the AM process. At first, AM was mostly used for prototyping products; however, it has evolved to produce finished products that are market ready.

There are many advantages to AM. First, it is a much more efficient process than more traditional methods of manufacturing. For instance, parts can move from design to production to testing much more rapidly in AM than in traditional manufacturing methods. Likewise, any required changes can be quickly implemented by adjusting the CAD [1]. Second, AM is particularly effective in producing objects with complex shapes that would be challenging to create by more traditional manufacturing methods [2]. Third, AM creates less material waste than more traditional manufacturing methods, reducing material waste by up to 87% in some applications [3]. With AM, only a small fraction of the material is not used in the finished product, and waste material can often be recycled for later use [4]. Fourth, AM can reduce the production cost of small batches, as it does not require the expensive upfront tooling and processing costs of subtractive manufacturing [2] [4].

There are also drawbacks to AM. First, the equipment costs can be a barrier to entry, with some industrial-grade 3D metal printers costing hundreds of thousands of dollars [5]. In addition, there are often additional costs for equipment set up, training of operators, and post-processing equipment to address flaws. Second, raw material costs for AM can be significantly more expensive than those in traditional manufacturing processes, as AM typically requires materials with fine particle distribution. Additionally, some AM processes can require the use of chemicals in either the production or clean-up stages, and those supplies add to overall costs. Third, AM build rates can be slow, making it less efficient for higher volume production runs. Fourth, the AM process can produce anisotropic parts, which can affect their ability to withstand high multi-directional stresses [2].

There are several technological advancements and trends that have sparked the growth in AM. Machine Learning (ML) is one of the advancements. ML enables a system to automatically analyze data and then use it to make future predictions and decisions [6]. ML can help adjust and improve process parameters, check the efficiency of in-process work, and assist in defect assessment.

The use of robots and automation is also helping to advance AM. Automation and robotic arms are critical features of 3D printers that allow consistent, continuous, and wide-range movement. Likewise, robots can operate continuously and are much more consistent than human workers, helping to reduce manufacturing costs [7].

AM is also enabling other industry trends including decentralized manufacturing. Since AM does not require as costly upfront tooling as traditional manufacturing, manufacturers do not have to rely on production in one dedicated location. Instead, AM relies on digital files that can be quickly and easily shared between multiple locations to meet customer demands when and where they occur. AM is also part of the growing green manufacturing trend in that it uses less raw materials and produces less waste [8].

There are seven forms of AM [8], which are described below. Objects created via AM processes serve multiple industries to include consumer foods and products, electronics, medical, manufacturing, construction, automotive, and aerospace. The products produced range from textured, multi-colored topographical maps to medical implants to engine parts and wings for the aerospace industry.

The AM process that is used in this research involving thermal nondestructive evaluation (NDE) is material extrusion; however, the proposed NDE technique discussed later in this thesis might also be applicable in other types of AM processes because most processes involve the application of heat either during or after the process.

1.1.1 VAT Photopolymerization

One type of AM is VAT polymerization, which is a process in which ultraviolet (UV) light is used to cure liquid polymers. A laser is used to machine the material into the desired shape layer by layer. Each layer must be cured before the next one can be laid. Curing is typically done using a laser source and remote-controlled mirrors. Additionally, blades are often run over each layer to smooth the surface and remove any flaws before the next layer is laid [9]. This process can lack structural support, so support structures made of the same material as the part are often used to compensate. After the object is created, the

supports are removed, and any remaining resin is removed by soaking the object in a chemical bath. Then the object goes through a final curing process [1].

The advantages of this process are that it provides a high degree of accuracy and smooth surface. The major drawbacks are the lack of product strength and the need for involved post-processing and clean-up steps [1].

1.1.2 Material Jetting

In material jetting, droplets of material are deposited by a moving print head to build an object layer by layer. Each layer is cured by ultraviolet light. Several sets of printheads can be used to deposit different materials, with polymers being one of the most common due to their high viscosity [10]. Objects with more intricate designs may require support structures. These support structures are removed post-process by soaking the object in a water-based liquid [1].

The advantages of the material jetting process are that it produces precise and accurate parts with smooth surfaces. It can accommodate different materials and multiple colors in a single print. Disadvantages include that it is expensive, and the resin container needs frequent filling. Additionally, material jetted parts that have been UV-cured can become brittle and lose strength over time [8].

1.1.3 Binder Jetting

In the binder jetting AM process, 3D parts are created by combining a powder-based material and a binder. A roller is used to lay the powder-based material on the build platform, and then a liquid binder is applied by an inkjet print head to bond one layer to the next. The process continues until the part is finished. The part then needs to cure before it is removed from the powder [11]. Excess powder is removed with pressurized air. Post-processing requirements vary depending on the material used but can include sintering for metal parts. Likewise, colored prototypes may require coating to make the colors brighter.

Advantages of this process include that binder jetting is relatively fast and cost effective compared to other AM processes, and it can be used with several different types of materials to include polymers, sands, metals, ceramics, and composites. Disadvantages of the process are that parts created using this process can be brittle, which gives them limited mechanical properties [8].

1.1.4 Material Extrusion

Material extrusion is a type of additive manufacturing process in which a material such as a polymer filament or pellet is heated and pushed through a nozzle in a continuous stream. The nozzle moves from side-to-side, and the build platform moves up and down to create the layers. Temperature and chemicals are used to help adjust the level of bonding between layers [12]. Many types of materials can be extruded, with two of the most popular ones being polymers and plastics because they offer good structural support. In parts with more complex geometries, two types of materials are used: one to create

the 3D part, and another to create a temporary support structure. The support structure is removed with chemicals after the part has been created [1].

In addition to working with a variety of materials, another main advantage of material extrusion is that it is economical. In fact, it is often used in inexpensive home 3D printers. It can also create fully functioning parts. Disadvantages include that it is one of the slower types of additive manufacturing processes, it is not as effective with fine details as other AM methods, and it has limited layer thickness accuracy. The larger the diameter of the nozzle, the lower the level of accuracy in the produced part [8].

1.1.5 Powder Bed Fusion

In the powder bed fusion process, fine powders are spread out on the design platform with a roller or blade and then fused together by a heat source. Two common heat sources for this process are electron beams and lasers. This process is continued layer by layer until the 3D part is completed. There are several variations of powder bed fusion such as direct metal laser sintering, selective laser sintering, multi jet fusion, electron beam melting, selective laser melting and selective heat sintering [13]. Depending on the level of support the powder surrounding the object provides, additional support structures may or may not be needed [1]. Post-processing requirements also vary, depending on the material and powder bed fusion process.

Powder bed fusion is another AM process that can create intricate designs with great accuracy and detail. Also, because there are so many variations of powder bed fusion, it works with a wide variety of metal and polymer materials. Some disadvantages of powder bed fusion are that it can take longer to complete than some of the other AM processes and that parts can lack strength [8].

1.1.6 Sheet Lamination

In this process, adhesive or ultrasonic welding is used to bind layers of material together. There are two basic forms of sheet lamination: ultrasonic additive manufacturing (UAM) and laminated object manufacturing (LOM). The difference between the two is mostly in the materials used and how they are bonded [1]. UAM uses ultrasonic welding to bind materials together and is most often used with metals. LOM uses adhesive, a heated roller, and pressure to bind together material, and plastics are mainly used in this method. In either variation, material is placed on a cutting bed and then layers are applied and bonded using either adhesive or ultrasonic welding [1][14].

The advantage of sheet lamination is that it is relatively fast, low cost and can accommodate a variety of materials. While it is good for visual models, drawbacks include that it is not as accurate as some other AM methods, and it is not suitable for structural use. Likewise, post-processing is often needed [8].

1.1.7 Directed Energy Deposition

Directed Energy Deposition (DED) was originally designed to produce fully functional parts out of metals and to repair metal parts. In this process, material is melted using an electron beam or laser and

is then deposited onto the work surface through a nozzle. Once a layer hardens, another layer is deposited. This process is mostly used with metal powders or wires, but ceramics and polymers can also be used [15].

The advantage of this process is that it can create dense parts with detailed geometries. However, this process is not as ideal for creating precise parts compared to other AM processes and may require post-processing. Furthermore, it is one of the more complex AM processes, and its equipment requires significant space and comes with environmental requirements [1].

1.1.8 Conclusion

This thesis involves the nondestructive evaluation of 3D-printed parts produced by the Material Extrusion process. This AM process was chosen in part due to a partnership with a company that employs this process in their production line. Furthermore, this process was compatible with materials that provided the proper strength and support requirements for their products. Lastly, this process was easy to replicate in a lab setting due to its low equipment and material costs so that multiple tests could be performed for accurate results.

1.2 Quality Control Methods Employed in Manufacturing

A product's quality can impact the way a part looks, performs, and is accepted by end-users. Therefore, a rigorous quality control process is an important element in any manufacturing process to reduce defects, enhance efficiency, and minimize costs.

In AM, quality control is essential. The types of materials used in AM continue to rapidly expand and now span from polymers to living tissue. It is challenging to predict how parts produced with different materials and in different AM processes will perform, especially in terms of how they might react to various mechanical loads. With AM evolving so quickly, quality control methods are also evolving to address the needs in AM.

Quality control processes have been defined in different manners and are often linked to the stage of the product life cycle. For example, there are different methods that can be used in the pre-manufacturing stages, such as those that pertain to product design, process planning and inspection of incoming raw materials [16]. Likewise, there are quality control processes that address in-process manufacturing. The goal of in-process methods is to detect flaws during the fabrication process so that adjustments can be made to correct the issue before the part is complete. There are several methods of in-process monitoring, including rheometry, ultrasound, and spectroscopy analysis [17]. Finally, there are quality control processes that involve post-production analysis. These are tests designed to test a part's reliability to ensure it meets its design and mechanical specifications.

Within these three categories of quality control processes, there are two methods of performing quality assessment. This evaluation can be done by either the more traditional, destructive evaluation or a nondestructive evaluation (NDE) approach, with the latter gaining in popularity throughout the manufacturing sector. Although neither evaluation technique can guarantee that specimens will not fail, they help to reduce the likelihood that a failure will occur. Therefore, virtually every manufacturing company employs at least one of these techniques [17].

1.2.1 Destructive Quality Monitoring

There are many forms of the more traditional, destructive quality monitoring, which can be used to determine material properties of specimens. Some of the most common tests include tensile, compressive, fatigue, torsion, nick break, and creep testing. Each of these tests evaluate crucial material properties of specimens such as strength, hardness, and ductility. However, the specimens tested are not likely to be used after they have undergone testing since most of the tests will fracture, elongate, or weaken the specimens, making them useless unless remanufactured. Furthermore, industry is trending towards using more in-process monitoring for more efficient flaw detection and correction. Traditional manufacturing typically has large production runs, where destructive monitoring only impacts a small percentage of parts being produced, making it feasible and cost effective. AM production runs are usually smaller, where destructive monitoring can negatively impact production efficiency and cost [18].

1.2.2 Nondestructive Quality Monitoring

Nondestructive evaluation (NDE) is a measurement that is performed to inspect a specimen to check for flaws or variations that could affect its usability without modifying the specimen in any way. Technically speaking, humans use NDE every day by inspecting objects with sight. Through visual inspection, people can determine if an object has a hole in it, if it is cracked, or if it is beginning to rust. Using these principles, researchers developed the NDE methods for manufactured parts. Over the past three decades, the use of NDE has increased significantly. This process is commonly used in incoming material examination, during in-process monitoring of materials, for post-fabrication testing, and for testing of in-use structures and machines [19].

The greatest benefit of NDE is that the part is not altered during testing. In other words, the part can be used once it has passed the test. It is particularly valuable in AM, where production volumes are lower than in traditional manufacturing, as no specimens are sacrificed in the evaluation process. Also, since tested parts with no flaws can be put back into production, the exact material properties of that specimen are known. This knowledge can be valuable when building critical structures. One of the limitations of NDE is that it can be time-consuming and costly [20].

The research presented in this thesis utilizes NDE for post-process assessment for many of the advantages previously mentioned.

1.3 Review of Nondestructive Quality Monitoring for AM

There a variety of NDE methods used in AM, and these are categorized in a variety of different ways in literature. For the purposes of this thesis, NDE methods will be organized into five broad categories to include visual inspection, acoustic techniques, imaging, optical techniques and use of electromagnetic fields [21]. Each of these will be discussed below, as well as some of their sub-categories that can apply in nondestructive evaluation of extruded parts.

1.3.1 Visual inspection

Visual inspection encompasses defects that can be detected by the human eye using instruments such as cameras or endoscopes, and, as such, is effective at detecting flaws at the macroscopic level. It is widely

used as a simple, low-cost method to detect flaws such as surface defects, improper sizing, and poor-fitting joints during production. Liquid or dye penetrants can also be used to help find flaws that are more difficult to detect because the penetrant is wicked into small openings in the 3D printed part that would otherwise go unnoticed. After it is applied, any excess penetrant is removed, and a developing medium is applied to the surface of the part. If surface defects are present, any of the penetrant that is trapped in them will rise to the surface and will cause the developer to change color. Similarly, dyes can be used to color the surface of a 3D printed object, which is inspected for flaws under regular lighting conditions. The advantages of visual inspection are that it is simple and cost-effective. The drawbacks are that it is limited in the types of flaws that it can detect. For instance, it will not detect issues with porosity, moisture, voids, damaged filaments or variations in density [22].

1.3.2 Acoustic Techniques

Acoustic techniques cover a variety of methods to include acoustic emission, nonlinear acoustics, and ultrasonic testing. One commonly used technique that will be discussed in more detail is acoustic emission (AE). In this method, sensors are applied to the test specimen which is then placed under stresses and/or temperature changes. The sensor sends electrical signals to a computer, where the measurements are processed to pick up stress waves. The more damage a part contains, the larger its stress wave and the stronger its acoustic signal will be [23]. Such feedback is valuable in assessing structural integrity of the object.

AE was first used by Kaiser in the 1950's to detect deformation in metal samples. He discovered that a metal placed under stress would emit an acoustic signal when the stress exceeded the level of stress that had been previously applied to it, signaling that deformation was about to occur. His work, later referred to as the "Kaiser Effect", is credited for laying the foundation for the use of AE to determine a material's structural integrity [23]. In the 1960's, instrumentation improvements expanded the range of frequencies that could be monitored to the 100kHz to 1Mhz range [24]. This work was important because it meant that expensive, dedicated, sound-proof facilities were no longer needed for acoustic emission testing, making the technique much more practical. Considerable research was also initiated in the 1970's to demonstrate that AE was a viable means of detecting flaws in fiber-reinforced components. Studies found that monitoring emissions from laminates showed promise [25].

Since then, AE has been used to examine flaws in a number of different materials and applications. Some research has focused on establishing signal parameters for different types of flaws [26]. Other researchers were able to build on this work to distinguish between tensile and shear crack signals in steel [27]. In his research, Prosser found that the amplitude of acoustic signals decreases as they occur further from the source, while noises close to the object being tested produce higher amplitude signals. He concluded that relying on amplitude alone was not sufficient and other noises needed to be removed. Gong found he was able to remove some of the extraneous noise through additional filtering methods [28]. AE is used frequently today and is especially effective in situations where load-bearing structures require ongoing monitoring.

One of the advantages of AE is that it is a passive technique, while other methods are active in that the energy that they use to detect flaws is induced upon the specimen. Instead, in AE, energy within the part itself is used. This can be beneficial for parts that already have known flaws so that the NDE technique does not worsen the issue. An example of where AE could be beneficial is in testing bridge supports that may have cracks due to fatigue so that the cracks do not worsen due to external energy exchanges.

1.3.3 Imaging Techniques

High resolution imaging relies on electromagnetic radiation to detect and measure flaws at atomic and molecular levels. The most used imaging techniques include phased contrast X-ray radiography and X-ray tomography. Phased contrast imaging can be done in either a lab setting or in a specialized synchrotron center. There is also a sub-category of phase-contrast X-ray called propagation-based phase-contrast imaging. It uses both absorption and phase contrast principles to create a detailed image with defined edges and boundaries [29]. Absorption contrast X-ray imaging for medical use was discovered in the late 1800's by Roengen [30]. Over the next twenty years, industry began using X-ray technology more frequently for applications such as analysis of alloys. Through his work at General Electric, Coolidge improved the X-ray tube by increasing its power and making it more controllable in terms of penetration depth and intensity [29].

The principle of phase-contrast imaging was the next evolution in imaging. As radiation from an X-ray passes through a material, it creates refraction. That refraction was used to further improve the resolution and contrast between materials of different density. Early work in this area was pioneered by Bonse and Hart who developed the first crystal interferometer [31].

Further enhancements to image resolution and contrast were made by Goetz et al., who developed an analyzer-based imaging (ABI) approach. They created a filter to selectively analyze only certain X-ray beams [32]. Later research into medical applications showed the benefit of the ABI approach. Wagner et al. were able to use the technology to assess whether a medical implant had attached properly to a patient's bone [33].

Another important advancement in imaging was that of X-ray tomography, which compensated for the overlapping structures that are seen in more traditional X-rays by taking images from multiple angles. In 1979, a German company pioneered the use of X-ray computed tomography (XCT) to assess the integrity of rotor blades on helicopters. Industrial use of XCT became more popular in the late 1990's with its use in the automobile industry. The technology was successfully used to assess the integrity of aluminum castings in car engines [34]. The applications for nondestructive evaluation using X-ray computed tomography (XCT) have grown rapidly, both in the medical and industrial sectors. The advantage of XCT is that it is effective at detecting a wide variety of flaws to include fractures, voids, contamination, porosity, fiber misalignment, and nonuniformity in thickness. Its disadvantages are potential operator exposure to radiation and limited effectiveness in evaluating composite materials [22].

1.3.4 Optical Techniques

Another category of nondestructive testing involves optical techniques. While there are many different types of optical techniques, this thesis will discuss IR Thermography, THz testing, shearography and digital image correlation.

1.3.4.1 Infrared Thermography

In Infrared Thermography (IRT), the heat radiating from an object is captured by a thermal imaging camera and is converted to a temperature. Those temperatures are displayed on a screen as two-dimensional images in which colors correlate to temperatures. IRT can monitor heat emitted in the

infrared range of the electromagnetic spectrum, which is invisible to the human eye. Most thermal imaging cameras can capture temperatures that range from -20 to 500°C, and many can extend that range even further. The concept behind IRT in NDE is that most materials give off energy as they fracture resulting in a local change temperature before they fail. By evaluating temperature distributions, IRT helps to pinpoint locations within an object where that object might weaken and eventually fail. IRT can be a valuable tool in detecting many types of flaws to include internal cavities, delamination, foreign particles, variations in thickness, and corrosion [22].

There have been significant developments in the field of infrared thermography and its use in nondestructive testing. A compilation of some of the most relevant milestones was created by Vladimir Vavilov and Douglas Burleigh, and some of those are highlighted below [35].

The earliest reference to IR light was made in 1800 by Astronomer Sir William Herschel, who discovered that a spectrum of colors was created when sunlight passed through a glass prism. IR was applied in the mid-1930's when Nichols successfully evaluated hot rolled metals using an early IR radiometer [35]. In 1948, Parker & Marshall further advanced IR research by using an early device called a pyrometer to successfully measure the temperature distribution in railway brake blocks to determine the optimal block length that would reduce degradation [36].

In the 1980s, a number of scientists made major advancements in the field pertaining to better understanding of thermal waves, pulsed thermography and how this knowledge could aid in measuring thermal conductivity. Others developed the idea of thermal quadrupoles, which allowed engineers to mathematically model heat conduction [35].

The 1990s brought further refinement in algorithms to measure and characterize defects, exploration into the principles behind fatigue in parts, and the development of early IR computerized systems. All of these advancements facilitated the use of IRT in industrial applications. Between 2000 and 2010, commercial equipment utilizing IR for nondestructive analysis became available. Advancements also continued to be made in algorithms to analyze and process data and the development of new, portable devices. Likewise, there was significant exploration into pairing IR assessment with other nondestructive evaluation methods [35].

There are two different techniques of IRT. One is active infrared thermography, in which external energy is applied to the part, thereby increasing its temperature reading by creating internal heat-flow. Another technique is passive infrared thermography, in which no external source of heat is used. In the field of NDE, IRT continues to be valuable today.

For this thesis research, active infrared thermography is the method being utilized. In this method, an IR camera is used to survey a specimen that is heated in an oven. This research discusses using heat transfer principles in combination with IR technology to explore a nondestructive evaluation method that estimates the thermal conductivity of 3D printed parts.

1.3.4.2 Shearography

Shearography is another optical technique that examines strain concentration in a sample using coherent light or sound waves. It is often referred to as speckle pattern shearing interferometry. Shearography is a very simple method, and its equipment requires minimal space and setup. It is often used for online inspection and has widespread use in auto manufacturing, aerospace and power plants. One of its main

advantages is that it is able to shut out environmental noise. Shearography has evolved over the years. Early shearography relied on a cumbersome wet photographic process to develop images. Electronic shearography allowed real-time analysis by using an electronic sensor to capture and send data to a monitor. It has now largely been replaced by digital shearography, which relies on a digital camera to capture data, enabling a much higher resolution image [37].

The advantages of shearography are that its scan rate is fast, and the equipment is reasonably priced. Among its drawbacks are that it is not capable of detecting as many types of flaws as other nondestructive techniques and its detectability decreases as a sample's thickness increases [22].

1.3.4.3 THz Testing

Terahertz (THz) is nondestructive evaluation that uses magnetic waves that fall between the microwave and infrared light spectrum (.1 to 10 THz range). The advantage of THz testing is that it can evaluate materials that were previously unable to be analyzed through NDE.

One type of system that incorporates this technology is the time-domain spectroscopy system, which uses short pulses of THz radiation to provide detailed characteristics of an object by analyzing intra- and inter-molecular interactions. This system is particularly valuable in thickness measurements [38].

The advantages of THz nondestructive testing are that its scan rates are fast, and the equipment is moderately priced. It is particularly valuable when working with low density materials. One drawback is that it is not as effective at evaluating composites as other methods [22].

1.3.4.4 Digital Image Correlation (DIC)

Another optical nondestructive method is digital image correlation (DIC). It works by generating 2D or 3D coordinates from the surface of an object based on recorded images from a single or series of cameras. It then measures local displacements between the coordinates to calculate data such as strain, deformities and contour. DIC has applications in structural health monitoring and is being widely used in civil engineering and other fields. DIC's advantages are that it works on a broad variety of materials, and it is more accurate than conventional equipment at measuring strain. It can also be a valuable tool in the areas of materials and component testing. Among its drawbacks are that it requires multiple steps, its results are highly dependent on the skills of the operator, and results are not always reproducible from one operator to the next [21].

1.3.4.5 Electromagnetic Fields

This method is used exclusively for conductive materials, and for this reason, it will only be briefly mentioned in this thesis. It utilizes electromagnetic induction to determine flaws in test specimens. While the technology is emerging, it is currently not widely used due its relatively high cost and lack of efficacy for composite materials [21].

1.3.5 Conclusion

IRT was chosen as the NDE technique for this research. In addition to its many advantages that have already been highlighted, it also has direct applicability in the transportation and aerospace industries. In

fact, it is currently used by both Boeing and Airbus for quality monitoring of their composite structures. This was particularly valuable because, as noted, much of the research in this thesis was done to support a company that produced 3D-printed shells for the automotive industry. Where the method studied in this research differs from methods previously employed is that the NDE IRT method employed here is used in conjunction with mathematical heat transfer models to give insight into specific material properties that can more accurately describe the issues related to flaws that are present in a part.

Chapter 2: Mathematical Approach

The ultimate goal of this research is to detect flaws in a 3D-printed specimen by characterizing variations in the thermal conductivity throughout the specimen through a nondestructive approach. The next section describes a mathematical method that uses a temperature estimation technique to compare experimental data to synthetic data created by the mathematical model. The first goal of this research is to determine if this technique can effectively determine the thermal conductivity of a specimen. If the thermal conductivity that is estimated is not consistent with the model, this inconsistency might be due to a flaw that is present.

The mathematical approach and derivation used in this research was similar in nature to that used in the Ph.D. dissertation of the Vanderbilt University graduate student Christopher Nash. He and the author of this thesis worked jointly on developing the mathematical approach used in both projects [39].

2.1 Heat Transfer Equations

To develop the heat transfer equations used to describe the cooling process of a specimen, the first law of thermodynamics was used. Given the experimental procedure that was used in the cooling tests, it can be assumed that no mass transfer took place and that heat transfer due to radiation was negligible. The heat loss can be attributed solely to the part being cooled by the surrounding air. As such, the process can be modeled using this equation:

$$\rho C_p \frac{\partial T(\mathbf{x}, t)}{\partial t} = \nabla \cdot (k \nabla T(\mathbf{x}, t)), \text{ for } \mathbf{x} \in \Omega, \quad (2.1)$$

where \mathbf{x} is the position vector, t represents time, ρ is the density of the specimen, C_p is the specific heat capacity of the part, and k is the thermal conductivity of the specimen. T is defined as temperature, which is a function of position and time, and ∇ is the gradient operator. There are likely to be small variations in local material properties in any engineered specimen depending on the way they are manufactured; however, these differences are assumed to be small and negligible.

The forward in time, centered in space (FTCS) finite difference approximation assumes that the material can be described using effective thermal conductivities that do not change over time or with temperature. Similar mathematical methods have been useful in other research, including in the cure monitoring of thermoplastic. The 3D domain that was considered is shown in Figure 2.1.

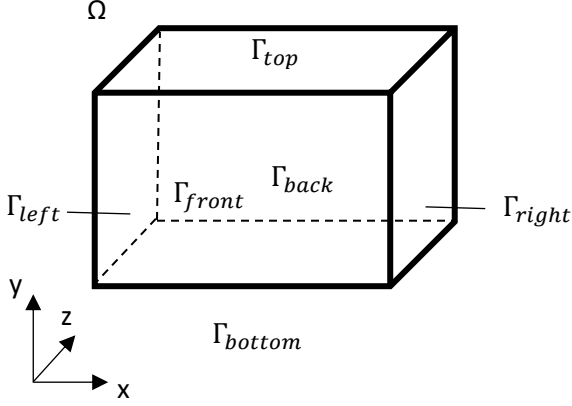


Figure 2.1: 3D domain (Ω) of specimens used in FTCS model

For a homogeneous material, the thermal conductivity was assumed to be the same in the x-, y-, and z-directions. The initial conditions and boundary conditions are described using the following equations:

$$(\mathbf{k}\nabla\mathbf{T}) \cdot \mathbf{n} = h(\mathbf{T} - T_{surr} \cdot \mathbf{e}_{ID}), \text{ for } \mathbf{x} \in \Gamma_{top} \cup \Gamma_{bottom} \cup \Gamma_{right} \cup \Gamma_{left} \cup \Gamma_{front} \cup \Gamma_{back}, \quad (2.2)$$

$$\mathbf{T}(\mathbf{x}, 0) = T_{init} \cdot \mathbf{e}_{ID}, \forall \mathbf{x}. \quad (2.3)$$

where T_{surr} is the temperature of the surrounding air, T_{init} is the initial temperature of the specimen, and h is the convective heat transfer coefficient. The vector \mathbf{e}_{ID} is a vector of ones with the same length as \mathbf{T} . All boundaries are convective boundaries with the surrounding air. One commonly used mathematical equation used for the heat equation is the FTCS finite difference approximation. The cooling of the specimen over time can be approximated using the FTCS approximation as given in this equation:

$$\mathbf{T}^i = \mathbf{M}\mathbf{T}^{i-1} + \mathbf{b}, \quad (2.4)$$

where \mathbf{M} is the diffusivity matrix, \mathbf{T}^i is the temperature vector containing the temperatures of all nodes at time step i , \mathbf{b} is a vector containing the boundary condition terms, and Δt is the time of the experiment. The full set of equations and specimen schematics can be found in Appendix A. These equations were programmed into a MATLAB code to compare synthetic data using the FTCS model to experimental data to estimate the thermal conductivity of the specimens.

2.2 Use of the Algorithm for Determining Thermal Conductivity

The specimens' temperature data over time was processed through a series of MATLAB codes that compare the experimental data to the FTCS model's synthetic data. The density, specific heat, part dimensions, initial temperature, and surrounding temperature were all input values that changed depending on the test and the specimen under investigation at the time. The initial and surrounding temperatures varied slightly due to changes over time in the experimental room and the oven. The room temperature for all tests was

approximately 23 degrees Celsius, and the oven temperature was approximately 80 degrees Celsius. All epoxy tests used a heat transfer coefficient of 4.95, which was determined through an iterative process, and all 3D-printed sample tests used a heat transfer coefficient of 10, which was reported by Rahman, et al. [40].

The FTCS model code created synthetic data using different combinations of thermal conductivity in the x-, y-, and z- directions. The rest of the variables in the FTCS model were held constant. Each experimental data set was then compared to the synthetic data for each thermal conductivity combination. The comparison code then outputted the thermal conductivity of best fit for the data set by choosing the thermal conductivity combination in the x-, y-, and z- directions that created the least error between the experimental and synthetic data. When using homogenous, isotropic materials the thermal conductivities in the x-, y-, and z-directions were assumed to be the same value. This constraint was included in the FTCS model so that only synthetic data produced by the same thermal conductivity values in each direction were tested. This constraint was lifted for the anisotropic case, as thermal conductivities are expected to change with direction. This method is discussed more in depth in Chapter 3.

Chapter 3: Materials and Methodology

This section discusses the different materials tested and the experimental process used to evaluate the proposed methodology described in the previous sections. The materials used became progressively more complex to assess if the methodology could estimate accurate thermal conductivities with each level of added complexity.

3.1 Materials

3.1.1 Epoxy

The first tests investigated a material that was homogeneous and isotropic. This type of specimen was chosen as a starting point since it had the simplest composition in which to determine the thermal conductivities in that there were no directional variations that were anticipated in the material properties. Epoxy was chosen as the first material since it was a close approximation to being homogeneous and isotropic. According to industry evaluations, the thermal conductivity of epoxy should be in the range of 0.20 to 0.35 W/mK [40][41]. The dimensions were 0.1273 m x 0.1273 m x 0.0102 m. The proposed method working with epoxy would showcase that the method could work in a one-dimensional, homogenous, isotropic case.

3.1.2 Epoxy with Hole

The second tests focused on a material that was isotropic but had a known flaw to determine if the proposed method could determine the location of the flaw within the part. For example, if a hole was located near the top left corner of the part, the thermal conductivities produced in that area would be lower than those found within the rest of the part. To create this material, an identical epoxy block to that of the first test was made, and a 0.5-inch hole was drilled near a corner of the part. The epoxy block with the hole had the same dimensions as the epoxy block from the previous section. It was assumed that thermal conductivities farthest from the hole should produce similar thermal conductivities to an ideal epoxy block. Similarly, it was assumed that areas closest to the hole would experience a drop in the thermal conductivity.

3.1.3 3D-printed materials

The final tests focused on anisotropic materials, meaning the materials were produced in such a way that they were assumed to potentially have different thermal conductivities in the x-, y-, and z-directions. The specific material used was extruded Acrylonitrile butadiene styrene (ABS), which has a thermal conductivity of 0.1 to 0.2 W/mK [40]. The samples were the same dimensions of the previous two samples. All samples can be seen below in Figure 3.1.



Figure 3.1: Samples used in testing (from left to right: epoxy, epoxy with hole, and ABS)

3.2 Methodology

3.2.1 Preliminary Experimental Methods

When beginning this process, flash thermography was considered as the desired measurement approach for producing and recording a temperature gradient within the specimen. However, when analyzing the data produced from these tests, an unusual spike in the temperature data at the start of collection was observed. Furthermore, the specimen cooled far too quickly to be practical. To verify the temperatures that were being recorded, thermocouples were added to directly record the temperature within the part, and the tests were performed again using flash thermography. The thermocouples displayed that the temperatures recorded by the IR camera were significantly higher than the temperatures recorded by the thermocouples. It was discovered that the IR camera was picking up the light from the flash thermography and was mistaking the light for extremely high temperatures, resulting in data that were inaccurate. To mitigate this issue, the block was painted with a matte black finish to prevent reflections back into the camera. The test was performed again with the painted specimen, but the spikes were still observed. Therefore, flash thermography was deemed to be an ineffective method of measuring the heat transfer within these specimens.

The next testing method used was heating the specimen with a heat blanket. The specimen was placed on a heat blanket underneath the IR camera. The heat blanket was turned on high, and the IR camera recorded the increase in temperature over time. This method eliminated the reflection error experienced with flash thermography and was able to accurately display the temperatures over time, which was verified using thermocouples. Furthermore, this method was able to visibly show vacancies within specimens that had holes. The heat blanket method was determined to be a viable method for flaw detection in 3D-printed parts.

One of the drawbacks discovered of using the heat blanket method was that the method was mathematically difficult to model. Not only would the model need to account for the heat blanket rising in temperature for a portion of the experiment, but the boundary conditions were also complex and difficult to estimate. To address these issues, a method utilizing a heat soak oven was developed. This method had all the benefits of the heat blanket and also created a uniform starting temperature for the specimen and

boundary conditions that were straightforward to model. The heat soak oven method was chosen as the experimental method in this research.

3.2.2 Data Collection via the Heat Soak Oven Method

To accurately determine material properties using the nondestructive cooling process, the material's temperature gradient data must be obtained. This data can be obtained by heating or cooling samples and observing how the part's temperature changes over time. Data for experiments detailed in this thesis were obtained by heating test specimens and observing how the parts cooled over time.

Both isotropic and anisotropic specimens can be tested for thermal conductivity using the following procedure. Prior to the testing process, material properties of the components comprising the specimen were researched to determine typical melting points and thermal conductivity ranges of the specimen. These values provided an indication of how the specimen might behave while cooling. The thermal conductivity ranges for the specimens were also researched before testing. These values were needed for establishing the actual expected thermal conductivities of the specimens and the errors in the estimates produced by the MATLAB code.

Specimens were selected based on their ability to withstand high temperatures (60 degrees Celsius to 80 degrees Celsius). A higher oven temperature allowed for a larger temperature gradient to develop during the cooling process, making it easier to obtain more information about the thermal properties of the specimen. Once melting point values were determined, an oven temperature was selected that was well below the melting temperature to prevent deformation of the specimen. The temperature chosen for experimentation for the specimens was 80 degrees Celsius. It was chosen because 1) it was below the melting temperature of all the specimens, and 2) it allowed for a large enough temperature to allow for a larger gradient while not melting any of the materials.

The materials used to collect the cooling data included a FLIR Infrared (IR) Camera, a mast arm holder for the IR camera, a computer able to operate the ResearchIR program, a programmable oven large enough to fit the specimen, a three-point stand to hold the specimen, gloves to place and remove the specimen from the oven, a table to house all the equipment, and the specimen being tested. Additionally, the test required a temperature-controlled room set at approximately 23 degrees Celsius.

The stand chosen for experimentation was selected to limit contact with the specimen as much as possible. If there were too many points of contact between the stand and the specimen, this estimation would have been inaccurate and would have produced poor results. The most accurate results were obtained when using a three-point stand (all surfaces surrounded by ambient air excluding three pinpoint locations that support the specimen under the IR camera). The stand was made of a thermally insulating material to reduce heat transfer effects on the specimen. The FTCS model used boundary conditions to model how the thermal conductivity would affect cooling of the specimen over time. The boundary conditions used assumed the specimen was surrounded by air throughout the duration of its cooling process. With minimal contact, this estimate gave a close approximation to the actual thermal conductivity of the material.

ResearchIR was the program used to collect the cooling data with the FLIR IR camera. The camera was operated with the program, calibrated, and the stand was placed directly underneath the camera lens. To determine the correct positioning of the specimen and the nodal locations where the measurements would be taken, the part was placed under the camera before placing it in the oven to be heated. Nine nodal locations in a three-by-three network were used in testing. An example of this set up can be seen below in Figure 3.2.

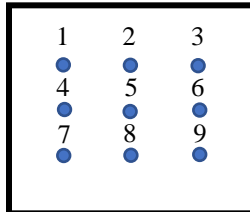


Figure 3.2: Nodal network example

Nine points were chosen to optimize efficiency while also gathering data about all boundary conditions. For instance, these nine nodal locations incorporated corner locations (areas that featured two boundary conditions), edge locations (areas that featured one boundary condition), and internal locations (areas that featured boundary conditions where no constraint as imposed). These points allowed data to be collected on the corner and edge boundary conditions, which helped to properly capture how the air surrounding the specimen factors into the cooling of the part, as well as an internal surface boundary condition, which is not exposed to the same air conditions.

Points, called Regions of Interest (ROIs), were placed at these nine nodal locations within the test specimen in the ResearchIR program. To account for any aleatory errors, such as slight variations in placement, each ROI took the average of the measurements at the four pixels surrounding the ROI to the north, east, south, and west. This average was then recorded in the system as the temperature at that point as a function of time.

Before temperature data was collected, the specimen was placed inside the oven for time periods spanning from 30 minutes to 60 minutes to allow the specimen to reach 80 degrees throughout so that each nodal location began at the same temperature when data collection commenced. These duration periods were found to be effective for the given specimen sizes. Lights in the room were also turned off to reduce reflectivity from the specimens that could potentially interfere with data collection through the IR camera. Once at a uniform temperature, the specimen was placed under the camera and the recording began. The times taken to remove the part from the oven and place the part under the camera were recorded and factored into the synthetic data to compensate for heat loss during the transfer period. Cooling data was collected for a duration of 20 minutes. Shorter time periods did not result in the temperature plateauing to room temperature, which meant that temperature gradients were excluded from the data set. Longer time periods equated to much longer data processing durations when analyzing the data. Therefore, 20 minutes was identified as the optimal duration. Set up of the IR camera and specimen can be seen in Figure 3.3.

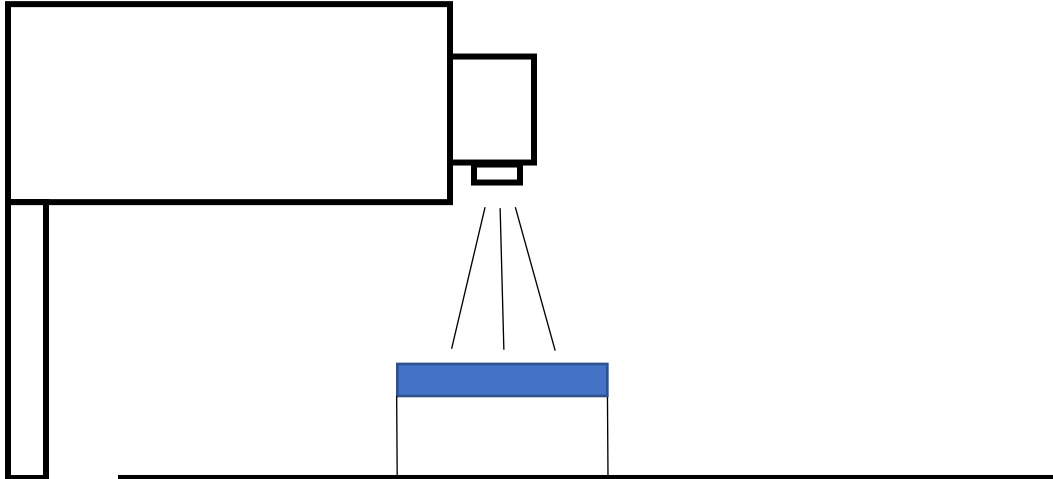


Figure 3.3: Schematic of IR camera and specimen experimental set up

Once the cooling data was collected, a temporal plot of the temperature versus time of the specimen was created in ResearchIR and saved as an .csv file to be compatible with MATLAB for data processing.

3.2.3 Data Processing Methodology

The temperature versus time data was converted to .mat files to be used in CompareFTCSandRealData code. Once processed into a useable MATLAB file, the data was passed through a low pass filter to reduce noise and to remove periodic jumps in data that arose from camera calibration during data collection. This filter allows data with low frequencies to pass through and prevents data with higher frequencies from being included in the data set.

Before running the CompareFTCSandRealData code, the FTCSModel code was run. This model used the FTCS equations to create synthetic cooling data that would be compared to the experimental data in the CompareFTCSandRealData code. The FTCSModel code ran through thermal conductivities ranging from zero (thermal conductivities cannot be lower than zero) to twice the industry accepted value for thermal conductivity of the material of the specimen (Note: a safety factor of two was chosen to make sure no thermal conductivities were missed). For instance, the range of epoxy thermal conductivities ranged from 0 to 0.80, increasing in increments of 0.01. Each set of cooling data corresponding to a different thermal conductivity would be compared to the experimental data in the CompareFTCSandRealData code to determine which thermal conductivities in the synthetic data best matched the experimental value. The thermal conductivity in the synthetic data that best matched the experimental data was recorded as the “true” value. Different combinations of four nodal locations were grouped together and processed using the CompareFTCSandRealData code to create a distribution of thermal conductivities for the specimen for each test. In total, each test had 126 thermal conductivity results.

The CompareFTCSandRealData code then plotted the synthetic data versus the experimental data for each different thermal conductivity synthetic data set within the range. The error was summed by adding the absolute value of the difference in temperature between the synthetic and experimental data over time. The code then provided the thermal conductivity that resulted in the lowest error. This value was the thermal conductivity of best fit for the specimen.

Chapter 4: Results

This section discusses the results obtained using the FTCS IRT method. A series of statistical tests were used to analyze the data to determine if this method could be a viable option for determining the thermal conductivity of isotropic and anisotropic materials, as well as detecting and locating defects within the specimen. A test was deemed “successful” if the average thermal conductivity found by the FTCS IRT method fell within the industry standard values.

4.1 Epoxy

The first experiments used an epoxy block to determine if the FTCS IRT method produced accurate results for a homogeneous, isotropic case. The specimens were made from TotalBoat epoxy, which has a thermal conductivity typically between 0.2 and 0.35 $\frac{W}{mK}$ [41][42][43]. Two different experiments, each collecting 126 combinations of data sets, were performed using the same epoxy block with no known defects. The density of the epoxy used was 1050 $\frac{kg}{m^3}$, and the specific heat was 1,100 $\frac{J}{kg^{\circ}C}$ [44][45].

4.1.1 Epoxy Test 1

4.1.1.1 Statistical Parameters

For the first test on an epoxy block, the overall thermal conductivity of best fit was determined to be 0.2645 $\frac{W}{mK}$. This value was determined by taking each thermal conductivity of best fit from the data set and finding the sample mean using Equation 4.1:

$$\bar{X} = \frac{1}{n} \sum_{i=1}^n x_i, x > 0 \quad (4.1)$$

where n is the number of best fit thermal conductivities in the data set and x is the thermal conductivity of best fit for data set i . The variance and standard deviation were also found using Equations 4.2 and 4.3 and were found to be 0.2687 $\frac{W}{mK}$ and 0.0518 $\frac{W}{mK}$, respectively.

$$s_x^2 = \frac{1}{n-1} \sum_{i=1}^n (x_i - \bar{x})^2, x > 0 \quad (4.2)$$

$$s_x = \sqrt{s_x^2} \quad (4.3)$$

The sample distribution is plotted in Figure 4.1.

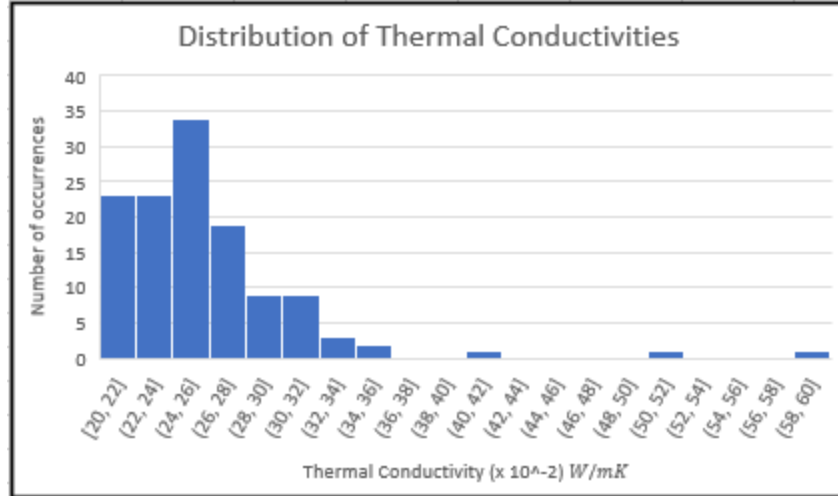


Figure 4.1: Frequency distribution of Epoxy Test 1

4.1.1.2 Probability Paper Tests

The sample distribution was investigated next. First, a probability paper test was performed on the data to determine which type of distribution fit the data best. Two distributions were tested: a Gaussian and a lognormal distribution. To construct a probability paper, the observed thermal conductivities were ranked from lowest to highest, where the ranking value was m . The observed thermal conductivity at rank m was then plotted at the CDF value of the rank number divided by the total number of thermal conductivities plus one, termed as the S values. The true S values for the normal and lognormal distributions can be found by using Equations 4.4, 4.5, 4.6, 4.7, and 4.8. A well-fitting distribution will plot a linear relationship between the S values created by the ranking and the thermal conductivity values. A poor fitting distribution would display a nonlinear relationship between the two variables.

$$S = \frac{x_i - \bar{x}}{s_x}, x > 0 \quad (4.4)$$

$$S = \frac{\ln(x_i) - \lambda_x}{\zeta_x} \quad (4.5)$$

where

$$\lambda_x = \ln(\bar{x}) - 0.5\zeta_x^2 \quad (4.6)$$

$$\zeta_x^2 = \ln(1 + \delta_x^2) \quad (4.7)$$

$$\delta_x = \frac{s}{\bar{x}} \quad (4.8)$$

The two probability papers after plotted in Figures 4.2 and 4.3.

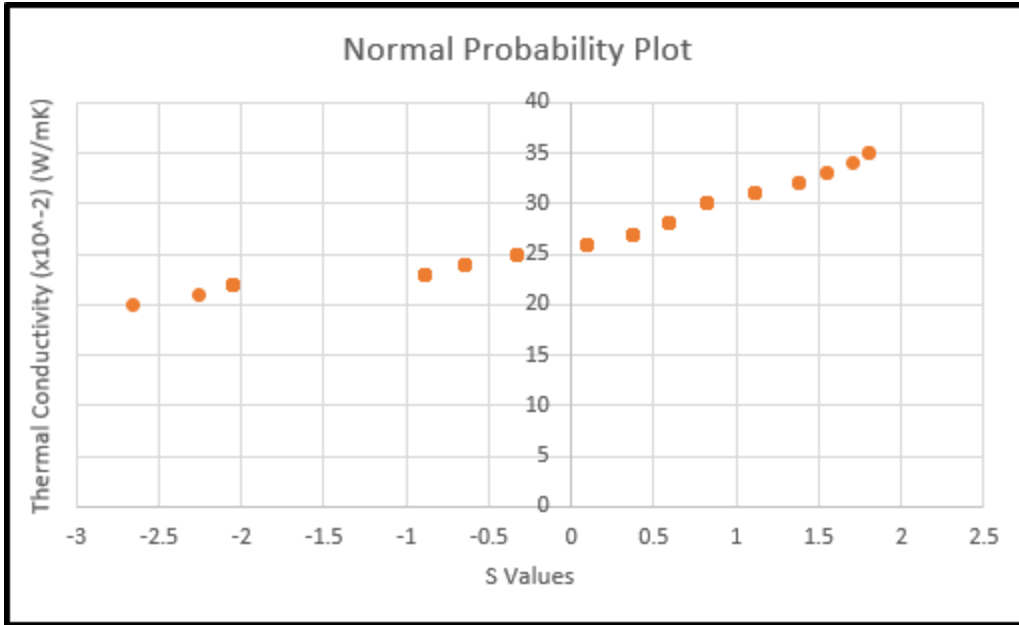


Figure 4.2: Normal probability paper for Epoxy Test 1

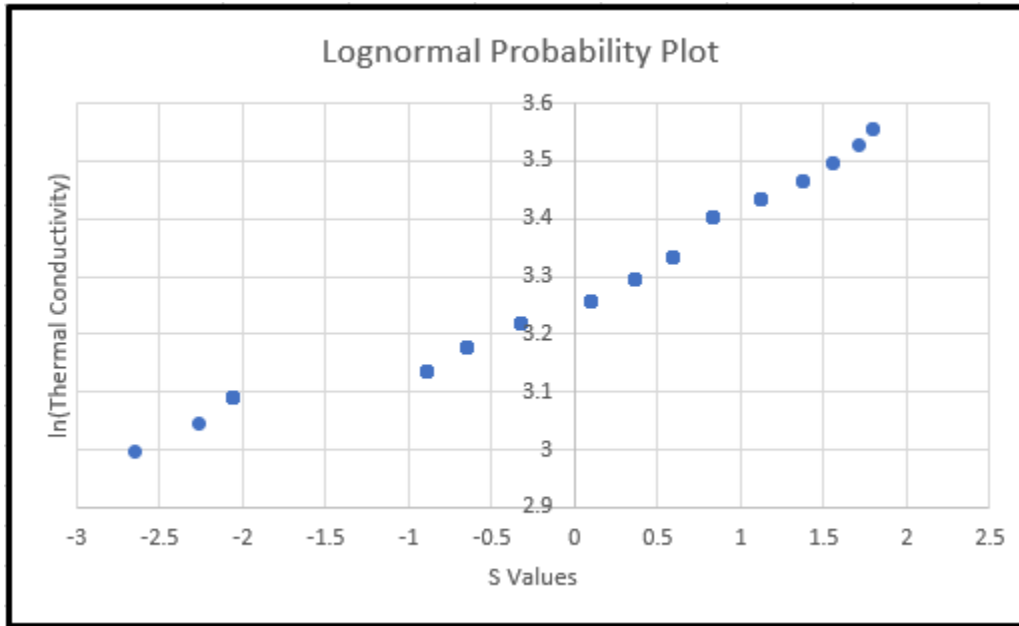


Figure 4.3: Lognormal probability paper for Epoxy Test 1

The distribution that had the most linear relationship using probability paper testing is the Gaussian distribution. To ensure that this distribution properly fit the data, a chi-square test and K-S test were performed.

4.1.1.3 Chi-Square Test

In the chi-square test, the thermal conductivity data was split into m bins of size two. The frequency for each bin was recorded, as was the theoretical frequency using a Gaussian distribution. If the value of the

square sum percent difference is lower than the chi-square statistic, C, with f degrees of freedom ($f = m - 1 - k$, where m is the number of bins and k is the number of parameters being estimated in the test) and $\alpha = 0.95$, then the distribution can be accepted. A summary of the results is tabulated in Table 4.1.

bins	Ni	Ei	(Ni-Ei)^2/Ei	C (f = 5, alpha = 0.95)
<22	23	24.4285	0.08353594	11.07
22-24	23	15.3685	3.78956661	
24-26	34	18.3986	13.2295058	
26-28	19	19.0146	1.1187E-05	
28-30	9	16.9644	3.7391177	
30-32	9	13.0659	1.26524451	
>32	8	17.7595	5.3632072	
sum	125	125	27.4701889	

Table 4.1: Results of chi-square test for Epoxy Test 1

Therefore, chi-square test shows that the Gaussian distribution should not be accepted.

4.1.1.4 K-S Test

In the K-S test, the experimental data's cumulative frequency is compared to the CDF of the Gaussian distribution. The data is arranged in an increasing order and numbered one through m, where m is the total number of data points. The Gaussian S values of the data points, F_E , are then compared the K-S test S values, found using Equation 4.9. The absolute value of the difference between the two S values, D_n , must be lower than the K-S test statistic D_n^α for the distribution to be accepted.

$$S_n(x_i) = \frac{m}{n}, x_m \leq x \leq x_{m+1} \quad (4.9)$$

For Epoxy Test 1, D_n was found to be 0.1776, and D_n^α was found to be 0.1216. Therefore, according to the K-S test, the Gaussian distribution is still not a good fit.

One reason why these two distribution tests may have failed is due to the presence of outliers in the data. An outlier test is performed below, and the tests were reproduced with the new data sets excluding any outliers.

4.1.1.5 Outlier Test

To determine if a data set contains outliers, the first quartile (Q1), third quartile (Q3), and interquartile range (IQR) of the data must be calculated. Once these values have been determined, the upper bound for the data, for which any data point greater than it is considered an outlier, can be found by multiplying the IQR by 1.5 and adding that value to Q3. Similarly, to find the lower bound of the data, the IQR is multiplied by 1.5 and subtracted from Q1. The results for Epoxy Test 1 are shown in Table 4.2.

Statistic	Value
QTL 1	0.23
QTL 3	0.28
IQR	0.05
Lower Limit	0.155
Upper Limit	0.355

Table 4.2: Results of outlier test

Three data points from Epoxy Test 1 were determined to be outliers exceeding the upper bound. The new data, excluding the three outliers, was reanalyzed.

4.1.1.6 Statistical Parameters Without Outliers

The new overall thermal conductivity of best fit was determined to be $0.2584 \frac{W}{mK}$, with a variance of $0.1094 \frac{W}{mK}$ and standard deviation of $0.0331 \frac{W}{mK}$. The new sample distribution is plotted in Figure 4.4.

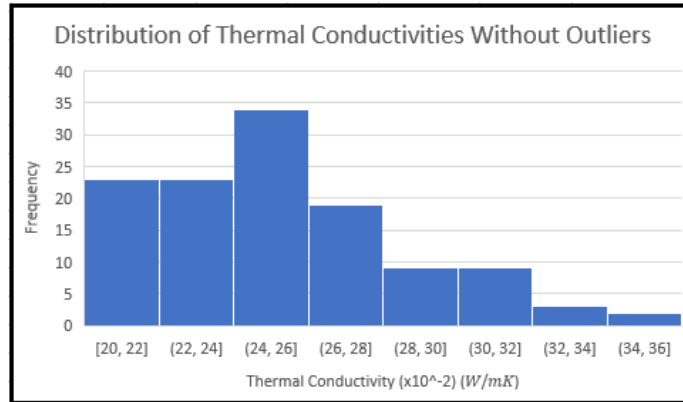


Figure 4.4: New frequency distribution of Epoxy Test 1

4.1.1.7 Probability Paper Tests Without Outliers

Like before, the sample distribution was investigated. First, a probability paper test was performed on the data to determine which type of distribution fit the new data best using the same process as before. Two distributions were again tested: a Gaussian and a lognormal distribution.

The two probability papers are plotted in Figures 4.5 and 4.6.

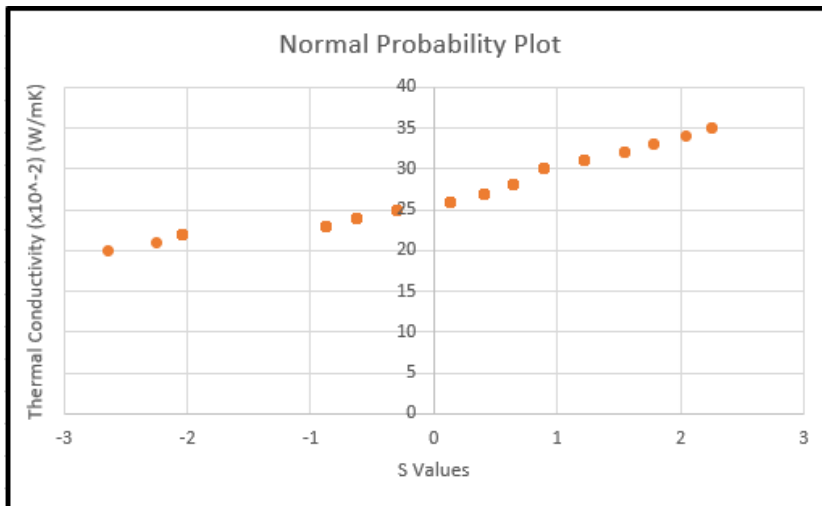


Figure 4.5: Normal probability paper for Epoxy Test 1

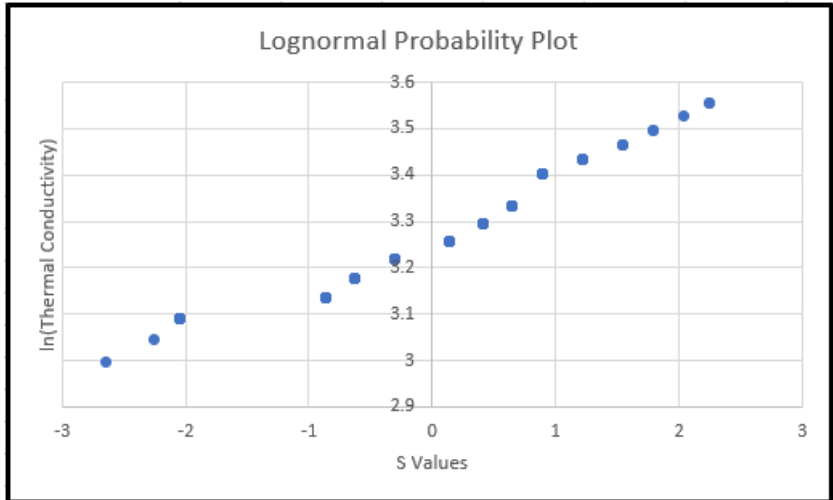


Figure 4.6: Lognormal probability paper for Epoxy Test 1

Both distributions produced fairly linear probability papers. To determine which distribution fit the data best, a chi-square test and K-S test were performed.

4.1.1.8 Chi-Square Test Without Outliers

The calculations for the chi-square test followed the same procedure as for Epoxy Test 1. The results of the chi-square tests can be seen in Tables 4.3 and 4.4.

bins	Ni	Ei	$(Ni-Ei)^2/Ei$	C (f = 5, alpha = 0.95)
<22	23	14.956125	4.326249947	11.07
22-24	23	20.251155	0.373121998	
24-26	34	28.0833	1.246553764	
26-28	19	27.318562	2.53302061	
28-30	9	18.64121	4.986421307	
30-32	9	8.9213574	0.000693243	
>32	5	3.8282917	0.358619593	
sum	122	122	13.82468046	

Table 4.3: Results of chi-square test for a Gaussian distribution for Epoxy Test 1 without outliers

bins	Ni	Ei	$(Ni-Ei)^2/Ei$	C (f = 5, alpha = 0.95)
<22	23	14.175857	5.492824409	11.07
22-24	23	22.848581	0.001003466	
24-26	34	29.363882	0.731973756	
26-28	19	25.707005	1.749869954	
28-30	9	16.54022	3.437373747	
30-32	9	8.2975582	0.059466219	
>32	5	5.0668967	0.000883218	
sum	122	122	11.47339477	

Table 4.4: Results of chi-square test for a lognormal distribution for Epoxy Test 1 without outliers

According to these results, the lognormal distribution fits the data best.

4.1.1.9 K-S Test Without Outliers

The K-S test was performed next. The D_n^α value for this data set was 0.1231. The Gaussian had a D_n value of 0.1499, and the lognormal had a D_n of 0.1267. Therefore, the lognormal continued to be the distribution of best fit.

4.1.1.10 Confidence Interval for Thermal Conductivity and Conclusions

While none of the tests perfectly fit the data, the lognormal will be used for the confidence intervals since it fit the data best for both tests. A 95% confidence interval was created using Equation XX:

$$\langle \mu \rangle_{1-\alpha} = \left[\bar{x} - t_{\alpha/2, n-1} \frac{s}{\sqrt{n}}; \bar{x} + t_{\alpha/2, n-1} \frac{s}{\sqrt{n}} \right] \quad (4.10)$$

where $t_{\alpha/2, n-1}$ is the Student t-distribution statistic and is approximately equal to 1.96. As such, the 95% confidence interval for Epoxy Test 1 without the outliers is $\left[0.2584 \frac{W}{mK}, 0.2643 \frac{W}{mK} \right]$, which falls within the industry range for the thermal conductivity of epoxy. Therefore, it was concluded that the FTCS IRT method produced accurate results for modeling thermal conductivities in homogenous, isotropic materials.

4.1.1.11 Comparison of the Nine Nodal Locations

The average thermal conductivities for combinations that contained each nodal point were then compared to observe any trends in the data. The distributions of the thermal conductivities for each node and their respective thermal conductivities are shown below in Figure 4.7.

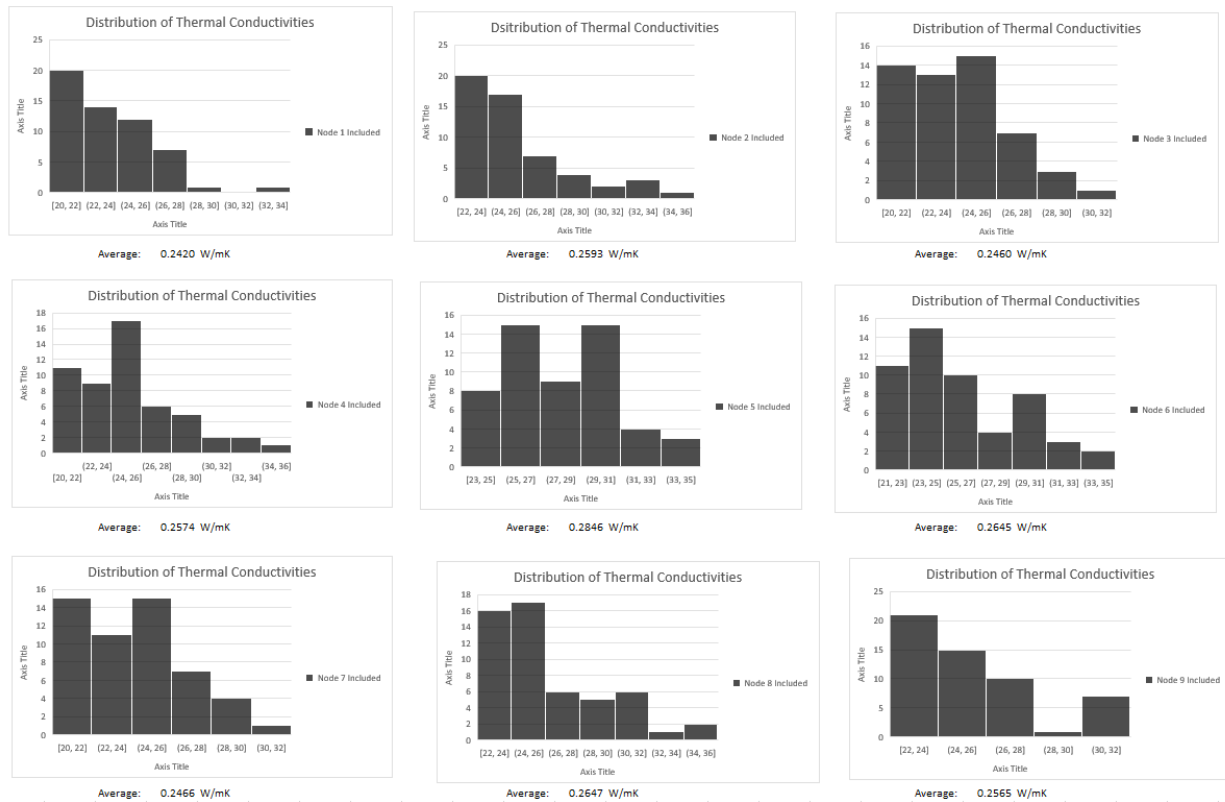


Figure 4.7: Frequency distribution for each node and its average thermal conductivity

The corners generate lower average thermal conductivities than the rest of the nodes. This observation makes sense, as the corners will cool at a faster rate compared to the rest of the nodes due to experiencing two boundary conditions from being exposed to the air. Additionally, the edge nodes (excluding the corners) generate thermal conductivities that are larger than the corner nodes, but less than the internal nodes. This observation also makes sense, as these nodes experience one boundary condition from being exposed to the air. Lastly, the internal node has the highest average thermal conductivity as no boundary condition constraint is imposed there.

4.1.2 Epoxy Test 2

4.1.2.1 Statistical Parameters

For the second test of the epoxy, the overall thermal conductivity of best fit was determined to be $0.2990 \frac{W}{mK}$. This value was determined the same way as in Epoxy Test 1 using Equation 4.1. The variance and standard deviation were also found using Equations 4.2 and 4.3 from Epoxy Test 1 and were found to be $0.4293 \frac{W}{mK}$ and $0.0655 \frac{W}{mK}$, respectively.

The sample distribution is shown in Figure 4.8.

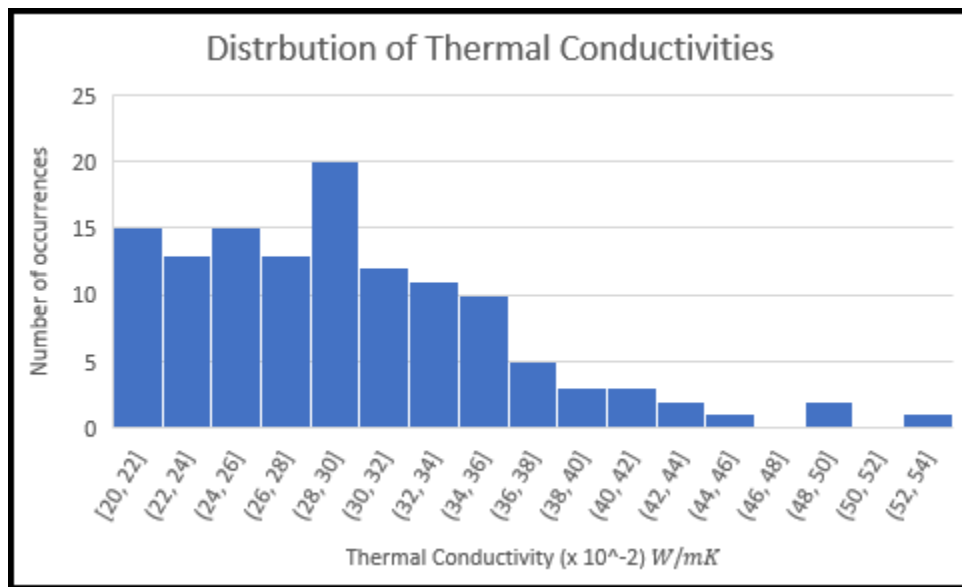


Figure 4.8: Frequency distribution of Epoxy Test 2

4.1.2.2 Probability Paper Tests

The sample distribution was investigated next. First, a probability paper test was performed on the data to determine which type of distribution fit the data best. Two distributions were tested: a Gaussian and a lognormal distribution. The construction of the probability paper plots followed the same process as in Epoxy Test 1. The three probability papers are plotted in Figures 4.9 and 4.10.

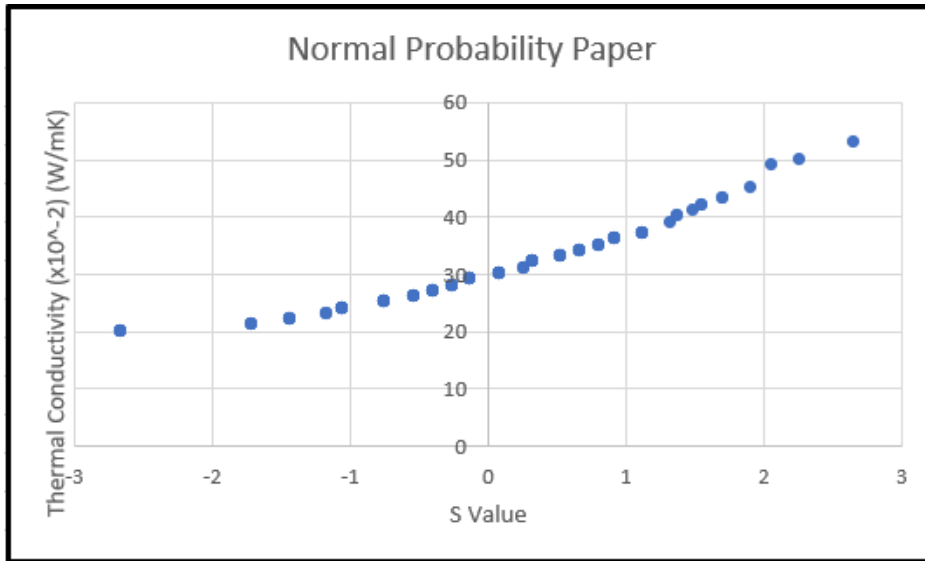


Figure 4.9: Normal probability paper for Epoxy Test 2

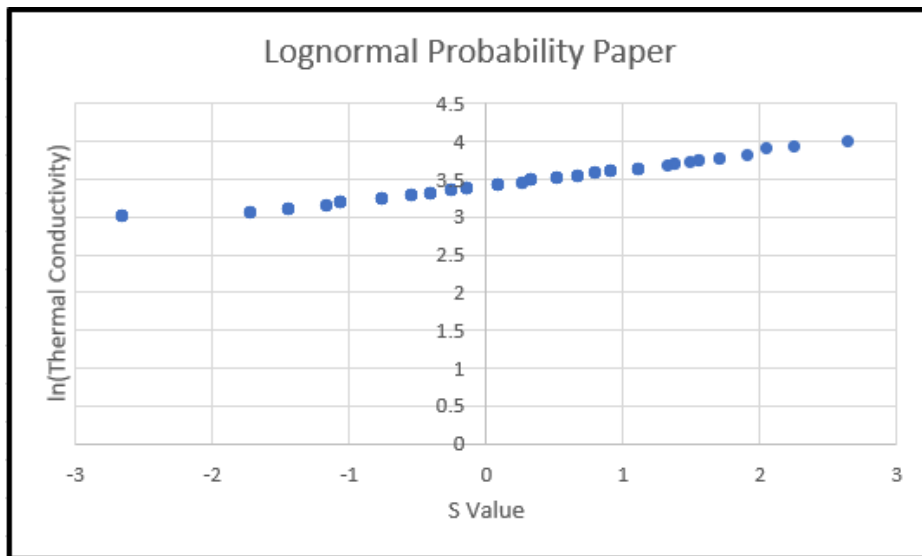


Figure 4.10: Lognormal probability paper for Epoxy Test 2

Both of the probability papers exhibit linear relationships. To determine which would have the best fit, a chi-square test and K-S test were performed.

4.1.2.3 Chi-Square Test

The calculations for the chi-square test followed the same procedure as for Epoxy Test 1. The results of the chi-square tests can be seen in Tables 4.5 and 4.6.

bins	frequency	Ei	(Ni-Ei)^2/Ei	C of 0.95,
<22	15	14.3146	0.032819788	15.51
22-24	13	8.79859	2.006216348	
24-26	15	11.5638	1.021097399	
26-28	13	13.856	0.052885537	
28-30	20	15.1367	1.56251314	
30-32	12	15.0758	0.627524809	
32-34	11	13.6893	0.528323609	
34-36	10	11.3328	0.156744063	
36-38	5	8.55354	1.476307896	
>38	12	13.6789	0.206057366	
sum	126	126	7.670489955	

Tables 4.5: Gaussian chi-square test results for Epoxy Test 2

bins	frequency	Ei	(Ni-Ei)^2/Ei	C of 0.95,
<22	15	11.96314	0.770909004	15.51
22-24	13	10.92811	0.392816623	
24-26	15	14.25964	0.038439692	
26-28	13	16.01174	0.566493779	
28-30	20	15.94024	1.033967196	
30-32	12	14.39599	0.39877434	
32-34	11	12.00743	0.084524431	
34-36	10	9.381262	0.040808617	
36-38	5	6.943554	0.544015521	
>38	12	14.1689	0.332005089	
sum	126	126	4.202754291	

Tables 4.6: Lognormal chi-square test results for Epoxy Test 2

From the chi-square test, both distributions technically fit the data, but the lognormal distribution fits the data best.

4.1.1.4 K-S Test

The K-S test was performed next. D_n^α value for this data set was 0.1212, and only the Gaussian distribution had an acceptable D_n value of 0.0979. The D_n value for the lognormal distribution was 0.0580. Therefore, the lognormal distribution was accepted as the distribution of best fit for Epoxy Test 2.

4.1.1.5 Confidence Interval for Thermal Conductivity and Conclusions

Since the lognormal distribution was accepted in all three tests, a 95% confidence interval was created using Equation 4.10 from Epoxy Test 1. The 95% confidence interval for Epoxy Test 2 is $[0.2877 \frac{W}{mK}, 0.3106 \frac{W}{mK}]$, which falls within the industry range for the thermal conductivity of epoxy. Therefore, it was

concluded that the FTCS IRT method continued to produce accurate results for modeling thermal conductivities in homogenous, isotropic materials.

4.1.1.6 Comparison of the Nine Nodal Locations

Like the first section, the average thermal conductivities were investigated at each of the nine nodal locations. The distributions are plotted in Figure 4.11.

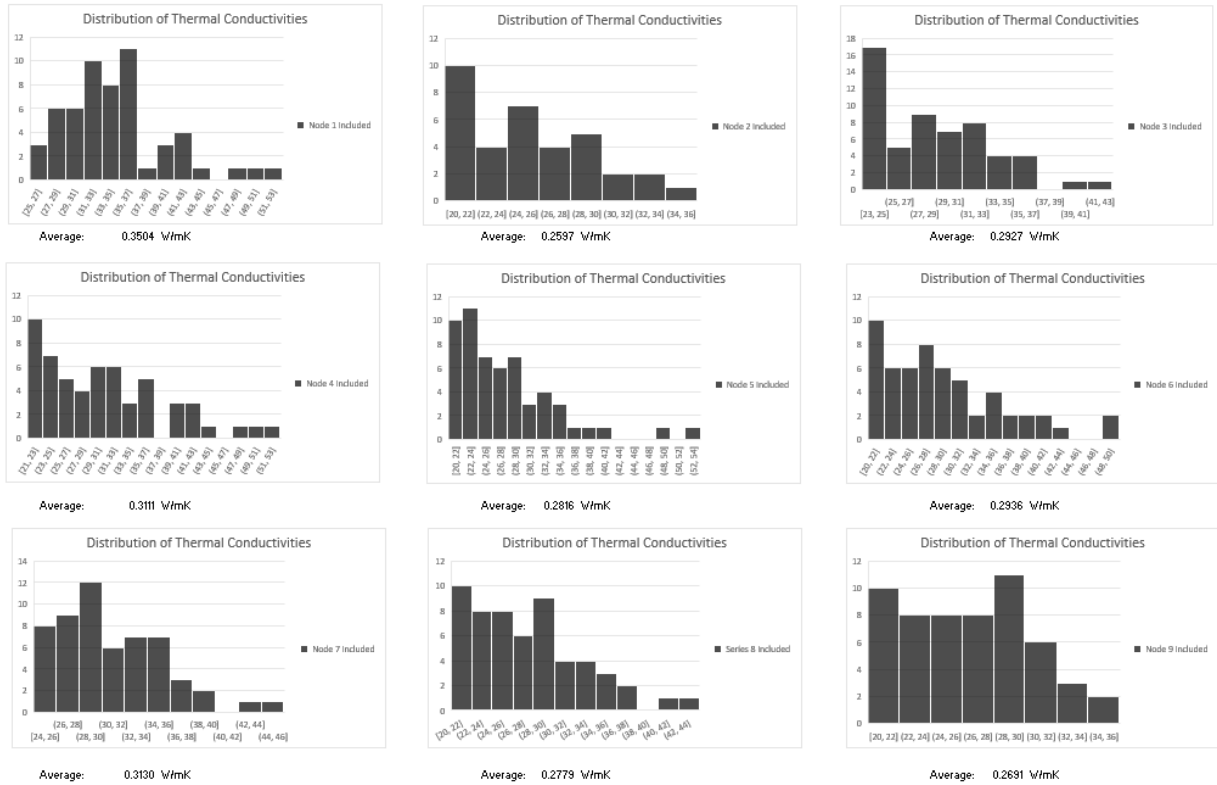


Figure 4.11: Frequency distribution for each node and its average thermal conductivity

Compared to the distributions from Epoxy Test 1, these distributions display no obvious trends. The differences can be attributed to how the part was removed from the oven or unexpected heating/cooling from the testing environment.

4.2 Epoxy with Hole

The second set of experiments used an epoxy block with a hole near node one to determine if the NDE FTCS method could detect that the thermal conductivity of the part near the hole decreased. The specimens were again made from TotalBoat epoxy, which has a thermal conductivity typically between 0.2 and $0.35 \frac{W}{mK}$ [41][42][43]. For these tests, it is expected that the thermal conductivity of the specimen near the hole will be lower than the thermal conductivity of specimen further away from the hole. As in the first two epoxy tests described in the previous section, two different experiments, each collecting 126 combinations of data sets, were performed using the same epoxy block. The density of the epoxy used was $1050 \frac{kg}{m^3}$, and the specific heat was $1,100 \frac{J}{kg^{\circ}C}$ [44][45].

4.2.1 Epoxy Hole Test 1

4.2.1.1 Statistical Parameters

For Epoxy Hole Test 1, the overall thermal conductivity of best fit was determined to be $0.2539 \frac{W}{mK}$. This value was determined the same way as in Epoxy Test 1 using Equation 4.1. The variance and standard deviation were also found using Equations 4.2 and 4.3 from Epoxy Test 1 and were found to be $0.1096 \frac{W}{mK}$ and $0.0331 \frac{W}{mK}$, respectively.

The sample distribution can be seen below in Figure 4.12.

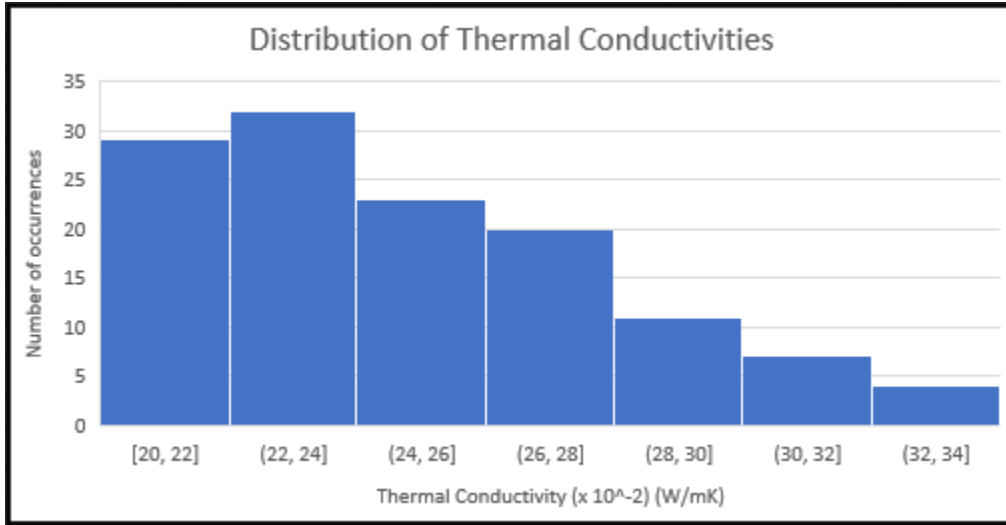


Figure 4.12: Frequency distribution of Epoxy Hole Test 1

4.2.1.2 Probability Paper Tests

The sample distribution was investigated next. First, a probability paper test was performed on the data to determine which type of distribution fit the data best. Like the previous two sections, two distributions were tested: a Gaussian and a lognormal distribution. The construction of the probability paper plots followed the same process as in Epoxy Test 1. The two probability papers are plotted in Figures 4.13 and 4.14.

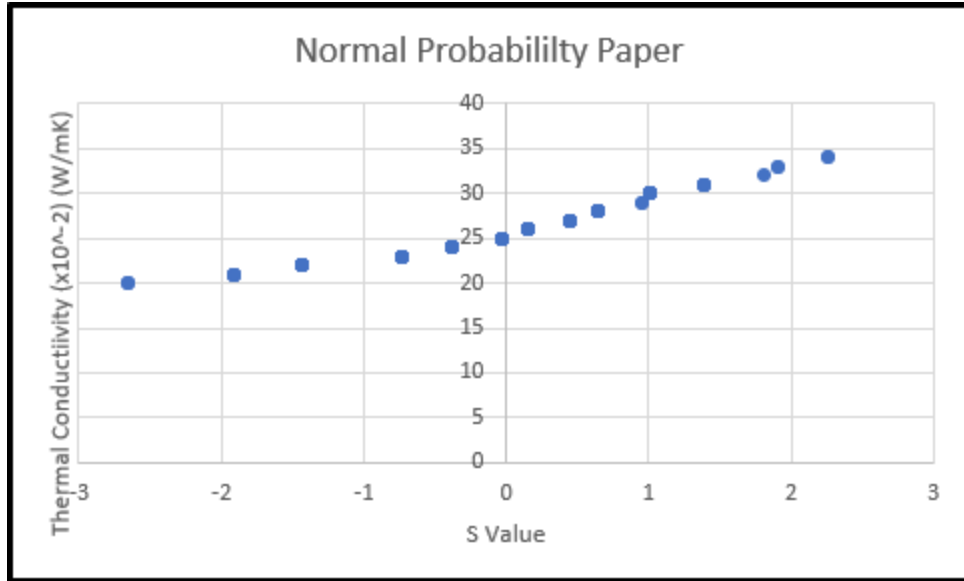


Figure 4.13: Normal probability paper for Epoxy Hole Test 1

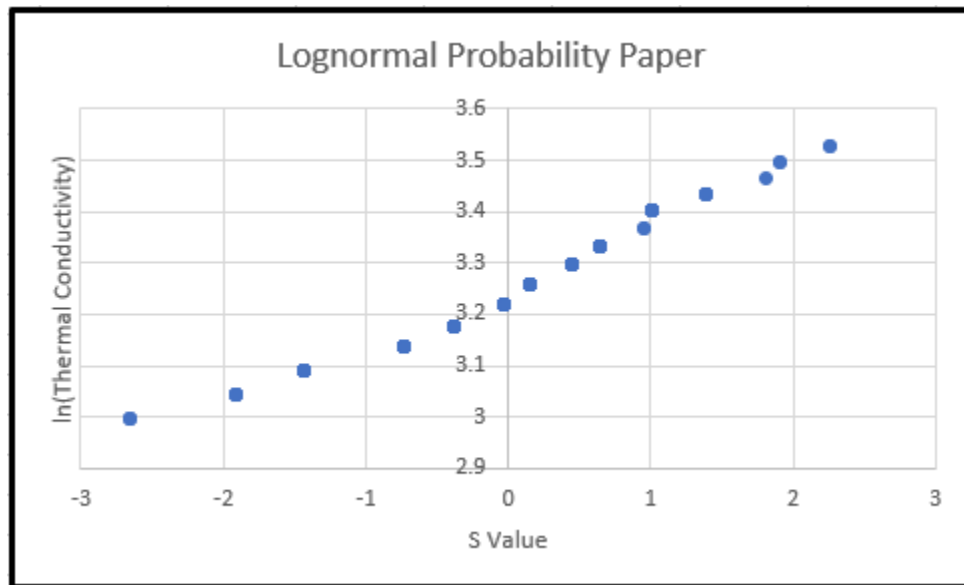


Figure 4.14: Lognormal probability paper for Epoxy Hole Test 1

In this test, two of the probability papers exhibited linear relationships: the Gaussian distribution and the Rayleigh distribution. To determine which would have the best fit, a chi-square test and K-S test were performed.

4.2.1.3 Chi-Square Test

The calculations for the chi-square tests followed the same procedure as the following two sections. The results of the chi-square tests are shown in Tables 4.7 and 4.8.

bins	frequency	Ei	(Ni-Ei)^2/Ei	C of 0.95
<22	29	19.2774	4.9036382	11.07
22-24	32	23.2365	3.3051181	
24-26	23	29.7128	1.5165653	
26-28	20	26.6664	1.6665495	
28-30	11	16.7964	2.0002967	
30-32	7	7.42362	0.0241739	
>32	4	1.53242	3.9734402	
sum	126	124.645	17.389782	

Table 4.7: Gaussian chi-square test results for Epoxy Hole Test 1

bins	frequency	Ei	(Ni-Ei)^2/Ei	C of 0.95
<22	29	18.83998	5.479089394	11.07
22-24	32	26.05446	1.356750994	
24-26	23	30.45012	1.822792945	
26-28	20	24.64458	0.875330046	
28-30	11	14.86303	1.00403426	
30-32	7	7.071093	0.000714773	
>32	4	4.076733	0.001444277	
sum	126	126	10.54015669	

Table 4.8: Lognormal chi-square test results for Epoxy Hole Test 1

From the chi-square test, the lognormal distribution is shown to fit the data better than the Rayleigh distribution.

4.2.1.4 K-S Test

The K-S test was performed next. The D_n^α value for this data set was 0.1212, and the Gaussian distribution had a D_n value of 0.1467. The D_n value for the lognormal distribution was 0.1278. Therefore, the lognormal distribution was shown to fit the data better with this test, as well.

4.2.1.5 Confidence Interval for Thermal Conductivity and Conclusions

A 95% confidence interval was created using Equation 4.10 from Epoxy Test 1. The 95% confidence interval for Epoxy Hole Test 1 is $[0.2481 \frac{W}{mK}, 0.2597 \frac{W}{mK}]$, which falls within the industry range for the thermal conductivity of epoxy.

4.2.1.6 Comparison of the Nine Nodal Locations

The purpose of testing the epoxy with the hole was to ascertain if this method could detect a change in a thermal conductivity when a flaw is present, resulting in a noticeable decrease in the thermal conductivity in the nodes closest to the hole. The frequency distributions for each node are shown in Figure 4.15.

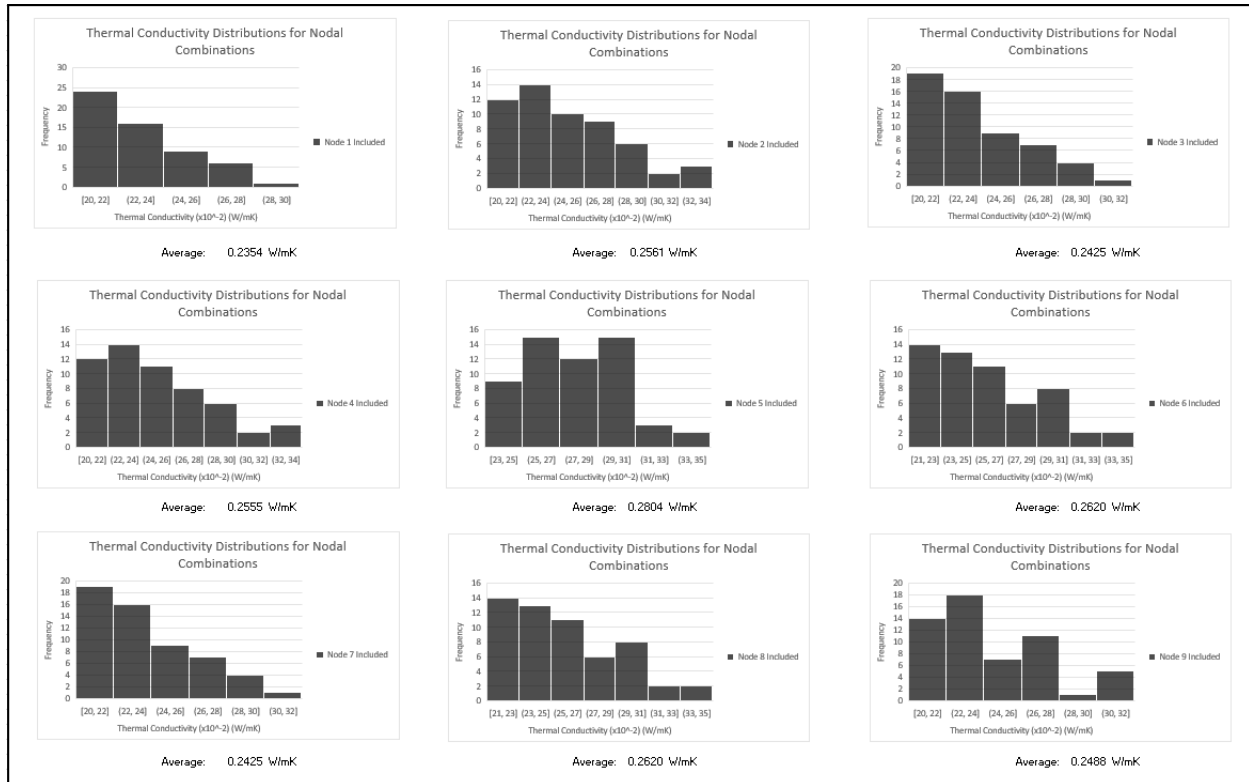


Figure 4.15: Frequency distribution for each node and its average thermal conductivity

The hole was placed closest to node 1, but was also located near nodes 2, 4, and 5. As anticipated, the lowest thermal conductivity was found near node 1, which is the node closest to the hole. It is also important to note that it was lower than all the other corner nodes which experience the same boundary conditions. Similarly, nodes 2 and 4 have lower thermal conductivities than nodes 6 and 8, even though they experience the same boundary conditions. Therefore, it was concluded that the FTCS IRT method was able to accurately detect a flaw through a change in local thermal conductivities.

4.2.2 Epoxy Hole Test 2

4.2.2.1 Statistical Parameters

For Epoxy Hole Test 2, the overall thermal conductivity of best fit was determined to be $0.2118 \frac{W}{mK}$. This value was determined using Equation 4.1. The variance and standard deviation were also found using Equations 4.2 and 4.3 from Epoxy Test 1 and were found to be $0.0501 \frac{W}{mK}$ and $0.0224 \frac{W}{mK}$, respectively.

The sample distribution is plotted in Figure 4.16.

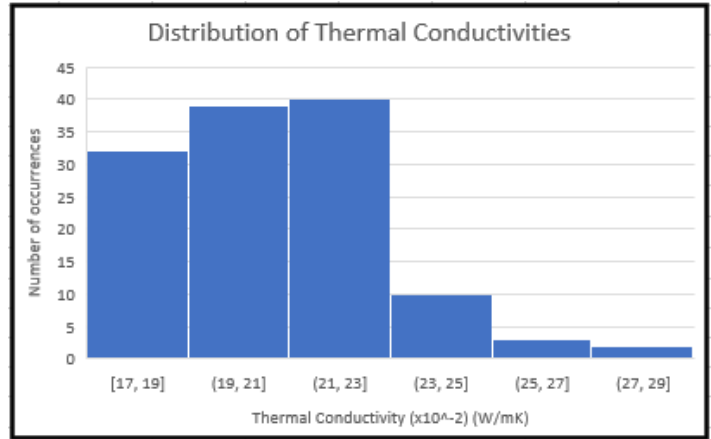


Figure 4.16: Frequency distribution of Epoxy Hole Test 2

4.2.2.2 Probability Paper Tests

The sample distribution was investigated next. First, a probability paper test was performed on the data to determine which type of distribution fit the data best. Like the previous three sections, two distributions were tested: a Gaussian and a lognormal distribution. The construction of the probability paper plots followed the same process as in Epoxy Test 1. The two probability papers are shown in Figures 4.17 and 4.18.

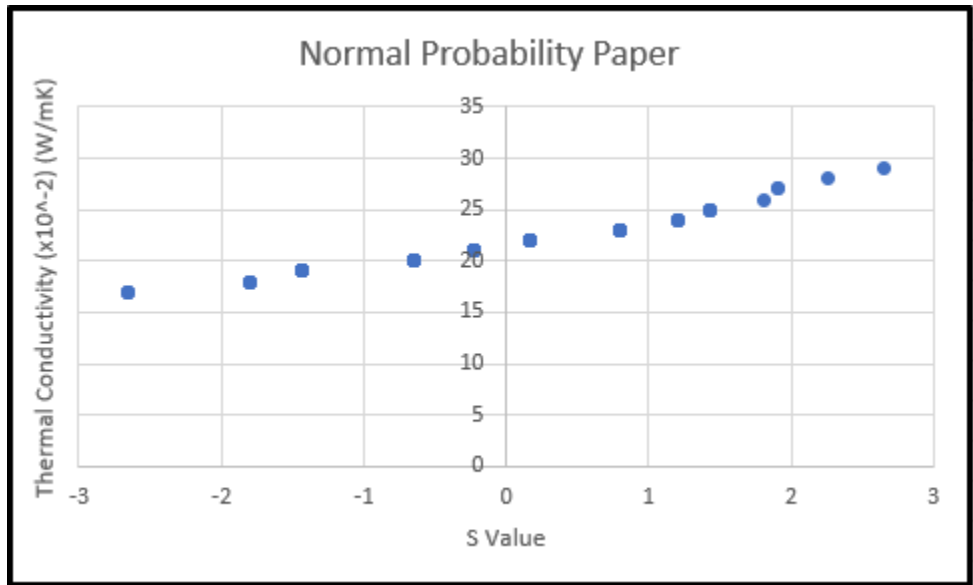


Figure 4.17: Normal probability paper for Epoxy Hole Test 2

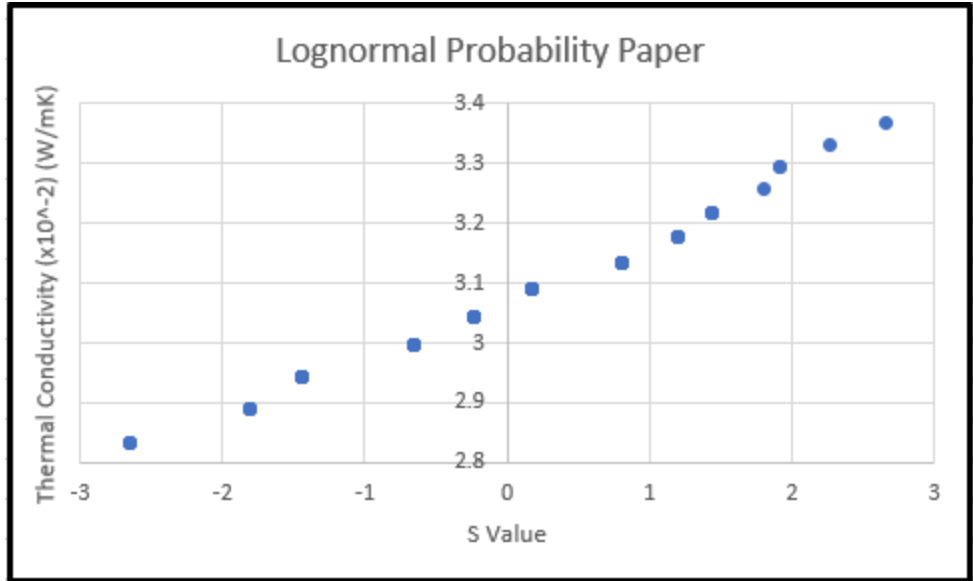


Figure 4.18: Lognormal probability paper for Epoxy Hole Test 2

In this test, the two distributions each exhibited fairly linear relationships. To determine which would have the best fit, a chi-square test and K-S test were performed.

4.2.2.3 Chi-Square Test

The calculations for the chi-square tests followed the same procedure as the following sections. The results of the chi-square tests can be seen in Tables 4.9 and 4.10.

bins	Ni	Ei	(Ni-Ei) ² /Ei	C (f = 5, alpha = 0.95)
<19	32	20.773	6.06776361	11.07
19-21	39	38.134	0.01966845	
21-23	40	40.822	0.0165354	
23-25	10	20.712	5.54046728	
25-27	3	4.9681	0.77966284	
>27	2	0.5909	3.36019658	
sum	126	126	15.7842942	

Table 4.9: Gaussian chi-square test results for Epoxy Hole Test 2

bins	Ni	Ei	(Ni-Ei) ² /Ei	C (f = 5, alpha = 0.95)
<19	32	20.739	6.11485137	11.07
19-21	39	40.803	0.07967173	
21-23	40	38.901	0.03105644	
23-25	10	18.932	4.21371566	
25-27	3	5.4377	1.09278616	
>27	2	1.1882	0.55471939	
sum	126	126	12.0868013	

Table 4.10: Lognormal chi-square test results for Epoxy Hole Test 2

From the chi-square test, the lognormal distribution was shown to fit the data best compared to the Gaussian distribution.

4.2.2.4 K-S Test

The D_n^α value for this data set was 0.1212. The Gaussian distribution had a D_n value of 0.1432, and the lognormal distribution had a D_n value of 0.1262. Therefore, the lognormal distribution was the distribution of best fit for this test, as well.

4.2.2.5 Confidence Interval for Thermal Conductivity and Conclusions

A 95% confidence interval was created using Equation 4.10 from Epoxy Test 1. The 95% confidence interval for Epoxy Test 2 is $[0.2079 \frac{W}{mK}, 0.2157 \frac{W}{mK}]$, which falls within the industry range for the thermal conductivity of epoxy.

5.2.2.6 Comparison of the Nine Nodal Locations

The distributions for each nodal location were investigated to determine if a flaw could be seen through the differing average thermal conductivities in the nine nodal locations. The frequency distributions for each node are shown in Figure 4.19.

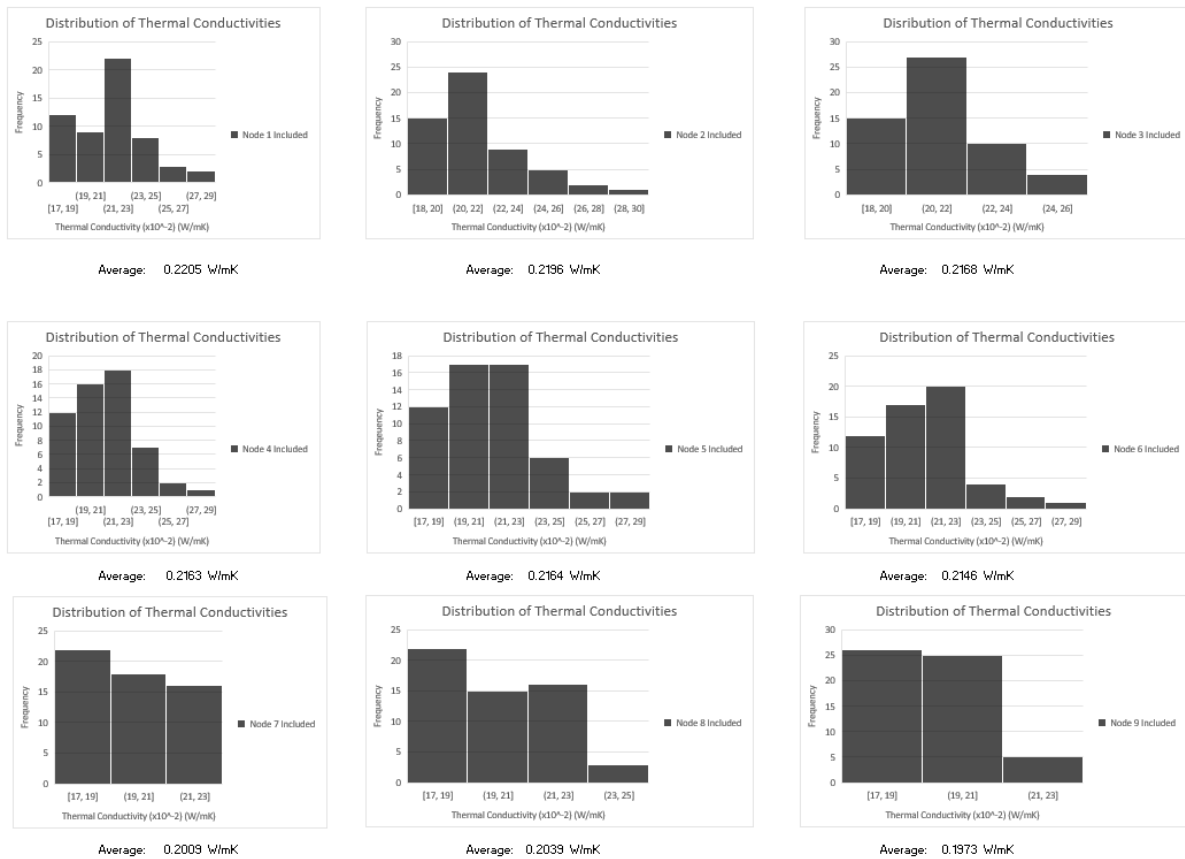


Figure 4.19: Frequency distribution for each node and its average thermal conductivity

The hole was placed closest to node 9 for this test, but was also located near nodes 5, 6, and 8. As anticipated, the lowest thermal conductivity was found near node 9, which is the node closest to the hole. Likewise, it was lower than all the other corner nodes which experience the same boundary conditions, as

was the case in the previous section. Therefore, it was concluded that the FTCS IRT method was able to accurately detect a flaw through a change in the output of thermal conductivities.

4.3 3D-Printed Specimens

The third set of experiments used an 3D-printed block to determine if the NDE FTCS method could determine the proper thermal conductivities of the part in the x-, y-, and z-directions. The specimens were made from ABS, which has a thermal conductivity typically between 0.1 and $0.2 \frac{W}{mK}$ [40].

Due to the nature of 3D-printed parts, there will always be gaps of air between beads and layers that are printed. While these gaps, along with bead-to-bead and layer-to-layer interfaces, can never be completely eliminated, learning how they affect the part's material properties is critical so that manufacturers can understand a part's behavior before putting it in a finished product. For these tests, it is expected that the thermal conductivity of the specimen will be different in every direction. Additionally, it is expected that the part will have an overall average thermal conductivity at the lower end of the range for ABS or slightly below. This is because the part will not be purely ABS, as described above. It will also feature gaps of air, bead-to-bead interfaces, and layer-to-layer interfaces that will slightly decrease the average thermal conductivity of the part since air has a lower thermal conductivity than ABS.

This test differed slightly from the last tests in that only certain nodal combinations were tested to save on computational effort and time. The number of synthetic models per run changed from 40 models in the last tests to 64,000 for the 3D-printed tests because the constant thermal conductivity constraint was relaxed. To create more reasonable run times and processing power requirements, certain combinations of nodes were chosen so that each node was represented equally, and each boundary condition was incorporated into the results. The density of the ABS used was $1050 \frac{kg}{m^3}$, and the specific heat was $1,400 \frac{J}{kg^{\circ}C}$ [40].

4.3.1 3D-Printed Specimen Test 1

For 3D-Printed Specimen Test 1, the overall thermal conductivity of best fit was determined to be $0.16 \frac{W}{mK}$ in the x-direction, $0.12 \frac{W}{mK}$ in the y-direction, and $0.04 \frac{W}{mK}$ in the z-direction. These values were determined the same way as in Epoxy Test 1 using Equation 4.1.

There was no change in the thermal conductivity output of the technique with change in nodal location. As such, the statistical tests performed on the previous tests would not be helpful in this case, as no useful information would be gained since the tests converged to one set value for the x-, y-, and z-directions. This result likely occurred due to the 3D-printed part having a relatively lower thermal conductivity and higher specific heat than other materials, such as the epoxy specimens that were used in the first two experiments. The cooling curves of the parts have a specific shape. When the thermal conductivity is changed in the model, it changes the shape of the synthetic data cooling curve. For instance, synthetic data using lower thermal conductivities have a more convex shape than those that have higher thermal conductivities. Since ABS has a relatively lower thermal conductivity and higher specific heat, the shape of the curve more heavily comes into play. This could explain why each of the tests produced the same result. It is very possible that the shape of the cooling curve produced by the combination of best fitting thermal conductivities matched the shape of the experimental cooling curve best, which is why this result occurred. Graphs of the experimental and synthetic cooling curves are shown in Figures 4.20, 4.21, 4.22, 4.23, and 4.24 to showcase these results, where the dashed lines are experimental data, and the solid lines

are synthetic data. From these plots, it is observed that the cooling curve that fits best is the one outputted by the technique, as it has the same shape as the experimental data.

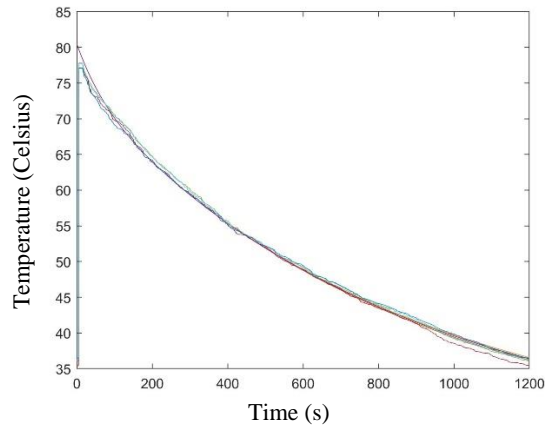


Figure 4.20: Comparison of experimental and synthetic data cooling curves ($k_x=0.16$ W/mK, $k_y=0.12$ W/mK, $k_z=0.04$ W/mK)

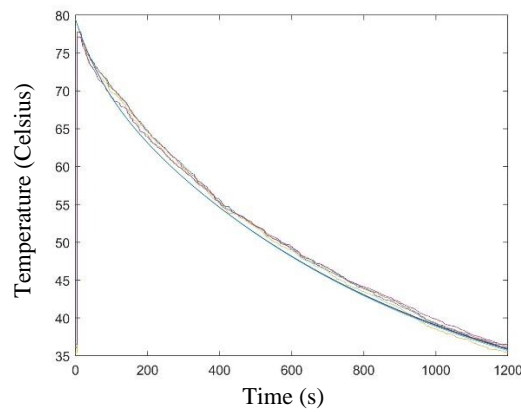


Figure 4.21: Comparison of experimental and synthetic data cooling curves ($k_x=0.13$ W/mK, $k_y=0.12$ W/mK, $k_z=0.04$ W/mK)

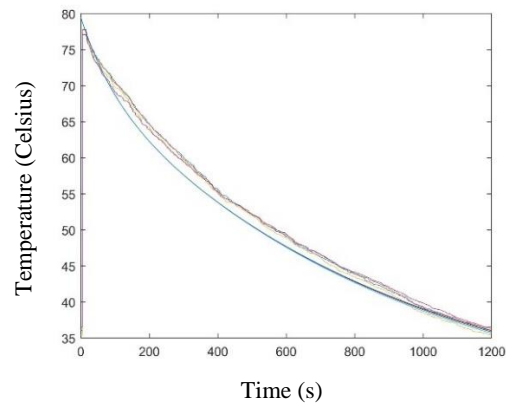


Figure 4.22: Comparison of experimental and synthetic data cooling curves ($k_x=0.16$ W/mK, $k_y=0.09$ W/mK, $k_z=0.04$ W/mK)

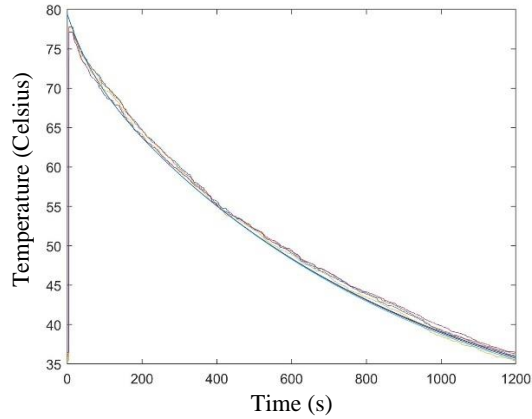


Figure 4.23: Comparison of experimental and synthetic data cooling curves ($k_x= 0.16$ W/mK, $k_y= 0.15$ W/mK, $k_z= 0.04$ W/mK)

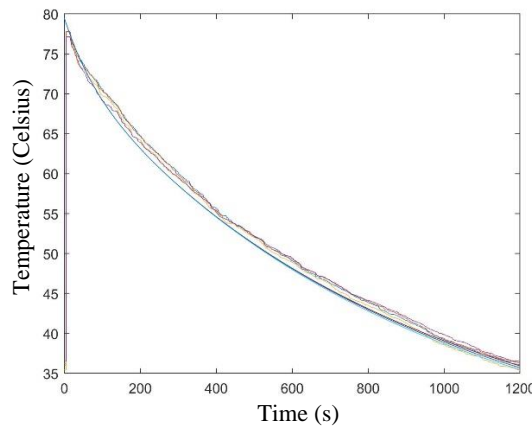


Figure 4.24: Comparison of experimental and synthetic data cooling curves ($k_x= 0.19$ W/mK, $k_y= 0.12$ W/mK, $k_z= 0.04$ W/mK)

4.3.2 3D-Printed Specimen Test 2

For 3D-Printed Specimen Test 2, the overall thermal conductivity of best fit was determined to be $0.0100 \frac{W}{mK}$ in the x-direction, $0.1738 \frac{W}{mK}$ in the y-direction, and $0.0138 \frac{W}{mK}$ in the z-direction. These values were determined the same way as in Epoxy Test 1 using Equation 4.1.

This method produced no variation in the x direction, and slight directions in the y- (variance = $0.003 \frac{W}{mK}$, standard deviation = $0.0052 \frac{W}{mK}$) and z-directions (variance = $0.011 \frac{W}{mK}$, standard deviation = $0.0106 \frac{W}{mK}$).

Similar to 3D-Printed Specimen Test 1, most of the combinations produced the same results for the average thermal conductivities in each of the three directions. This result was likely observed for the same reasons as 3D-Printed Specimen Test 1. When a part cools, it has a specific rate of change based on its thermal conductivity, density, and specific heat, among other properties and environmental conditions. This rate of change creates a distinct cooling curve with a distinct shape. The 3D-printed part has a relatively lower thermal conductivity and higher specific heat than other materials, such as the epoxy

specimens that were used in the first two experiments. When the thermal conductivity of the model changes, the shape of the synthetic data cooling curve changes, as well. For instance, synthetic data using lower thermal conductivities have a more convex shape than those that have higher thermal conductivities. Since ABS has a relatively lower thermal conductivity and higher specific heat, the shape of the curve more heavily comes into play. It is very possible that the shape of the cooling curve produced by the combination of best fitting thermal conductivities matched the shape of the experimental cooling curve best, which is why this result occurred.

4.3.3 Discussion on 3D-Printed Specimen Results

Between both tests, the y-direction thermal conductivity remained fairly consistent and within the industry range for ABS thermal conductivity. The y-direction represents the direction of the bead print on the surface layer. Since the specimen is anisotropic, the direction of the bead print changes from layer to layer. However, all data collection took place on the surface of the part, which could explain why the y-direction was more consistent and within the industry range. The direction of the bead print is much more homogenous than the other two directions because it experiences fewer bead-to-bead interfaces to cross along its length that would cause a drop in the thermal conductivity. Because the measurement took place on the surface of the part where this direction behavior would be observed, it would make sense that the y-direction would have thermal conductivity values that match that of ABS. A schematic of the part is shown in Figure 4.25.

Additionally, the z-direction thermal conductivity remained fairly consistent and slightly lower than the industry range between both tests. The z-direction represents the thickness of the part. The thickness direction experiences many layer-to-layer and bead-to-bead interfaces that cause drops in the thermal conductivity, making it much less homogeneous than the other two directions. As such, it would make sense that the z-direction would produce consistently lower thermal conductivity values.

The x-direction thermal conductivities were not consistent between the two tests. The large variations in thermal conductivity may be due to the changes of the bead print direction throughout the part. Further research is needed in the direction perpendicular to the bead print on the surface layer to better understand this behavior. It would also be helpful to analyze specimens that have the bead print all in one direction, or transversely isotropic specimens, to understand directional variations.

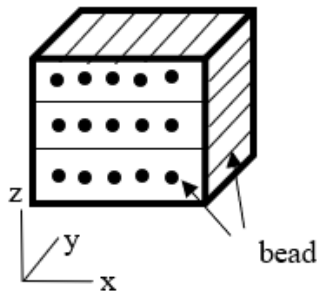


Figure 4.25: Schematic of the 3D-printed part

From this analysis, the algorithm-aided IRT NDE technique is a potentially viable method for determining the thermal conductivity of 3D-printed parts in the direction of the bead print on the surface layer and in the direction of the thickness. Further research would need to be completed to determine the viability of this method in the direction perpendicular to the bead print on the surface layer.

Chapter 5: Conclusion

This research investigated using an algorithm-aided IRT NDE technique to estimate the thermal conductivity of both isotropic and anisotropic parts to facilitate flaw detection. For isotropic materials, this method was able to produce thermal conductivities for the part that fell within the industry range for that part's material, verifying that this method is a viable means of accurately determining the thermal conductivity of isotropic parts. This new technique was also able to detect local differences in thermal conductivity where flaws were intentionally imposed in isotropic materials. As such, the algorithm-aided IRT NDE technique is a potentially viable option for material property testing and flaw detection in isotropic parts.

This method was able to produce consistent results in anisotropic 3D-printed specimens in the y- and z-directions. The y-direction, which was the direction of the bead print on the surface layer, was shown to consistently fall within the industry range for thermal conductivity of ABS. This result makes sense, as the direction of the bead print is more homogenous due to less bead-to-bead interfaces. Similarly, the z-direction, which represents the direction of the thickness, was shown to consistently be less than the industry range for thermal conductivity of ABS. This result makes sense because the direction of the thickness contains more layer-to-layer and bead-to-bead interfaces. The x-direction, which was the direction perpendicular to the bead print on the surface layer, was not consistent between tests. The variation in thermal conductivity may be due to the bead print direction changing from layer to layer. From this analysis, the algorithm-aided IRT NDE technique is a potentially viable method for determining the thermal conductivity of 3D-printed parts in the direction of the bead print on the surface layer and in the direction of the thickness. Further research would need to be completed to determine the viability of this method in the direction perpendicular to the bead print on the surface layer. It would also be helpful to analyze transversely isotropic specimens to better understand directional variations.

The epoxy with hole tests provided more insight than the other tests, in that it was able to show where flaws were present in the part. The algorithm-aided IRT NDE technique approach was able to detect the change in thermal conductivity where the hole was located. This shows the potential of this technique to detect the location of flaws within parts, since spatial variations were able to be accurately detected. In addition to performing further research to assess the viability of this method in determining the thermal conductivity of the specimen in the direction perpendicular to the bead print on the surface layer, it would be valuable to create and test 3D-printed parts with intentionally induced flaws to determine if this technique can identify the location of flaws in anisotropic parts based on changes in thermal conductivity.

References

1. Parupelli, S.K., Desai, S. A Comprehensive Review of Additive Manufacturing (3D Printing): Processes, Applications and Future Potential, *American Journal of Applied Sciences*, 2019: 16 (8): 244-272. DOI: 10.3844/ajassp.2019.244.272
2. Jiménez, M., Romero, L., Domínguez, I.A., Espinosa, M., Domínguez, M. Additive Manufacturing Technologies: An Overview about 3D Printing Methods and Future Prospects, *Complexity*, 2019: Vol. 2019, Article, 30 pages. ID 9656938. DOI: 10.1155.2019/9656938
3. Paris, H., Mokhtarian, H., Coatanea, E., Museau, M., Ituarte, I.F. Comparative environmental impacts of additive and subtractive manufacturing technologies, *CIRP Annals - Manufacturing Technology*, 2016: Vol. 65, 29-32. <https://doi.org/10.1016/j.cirp.2016.04.036>
4. Ford, S., Despeisse, M. Additive manufacturing and sustainability: an exploratory study of the advantages and challenges, *Journal of Cleaner Production*, 2016: Vol. 137, 1573-1587. <https://www.sciencedirect.com/science/article/pii/S0959652616304395>
5. Metal 3D printers in 2021: a comprehensive guide <https://www.aniwaa.com/buyers-guide/3d-printers/best-metal-3d-printer/>
6. Wang, C., Tan, X.P., Tor, S.B., Lim, C.S. Machine learning in additive manufacturing: State-of-the-art and perspectives, *Additive Manufacturing*, 2020: Vol. 36, 101538, online.
7. Mineo, C., Pierce, S.G., Nicholson, P.I., Cooper, I. Robotic path planning for non-destructive testing – A custom MATLAB toolbox approach, *Additive Manufacturing Trends*, 2016: Vol. 37, 1-12. <https://www.additivemanufacturing.media/kc/what-is-additive-manufacturing/additive-manufacturing-trends>
8. Tofail, S.A., Koumoulos, E.P., Bandyopadhyay, A., Bose, S., O'Donoghue, L., Charitidis, C. Additive manufacturing: scientific and technological challenges, market uptake and opportunities, *Materials Today*, 2018: Vol. 21 (1), 22-37.
9. Pagac, M., Hajnys, J., Ma, Q.P., Jancar, L., Jansa, J., Stefek, P, Mesicek, J. A Review of Vat Photopolymerization Technology: Materials, Applications, Challenges, and Future Trends of 3D Printing, *Polymers*, 2021: 3(4), 598; <https://doi.org/10.3390/polym13040598>
10. Yap, Y.L., Wang, C., Sing, S.L., Dikshit, V., Yeong, W.Y., Wei, J. Material jetting additive manufacturing: An experimental study using designed metrological benchmarks, *Precision Engineering*, 2017: Vol. 50, 275-285.
11. Mastafaei, A., Elliott, A., Barnes, J., Li, F, Tan, W., Cramer, C.L., Nandwana. P., Chmielus, M. Binder jet 3D printing—Process parameters, materials, properties, modeling, and challenges, *Progress in Materials Science*, 2021: 119, 100707. <https://www.sciencedirect.com/science/article/pii/S0079642520300712>

12. Somireddy, M., Czekanski, A. Anisotropic material behavior of 3D printed composite structures – Material extrusion additive manufacturing, *Materials & Design*, 2020: Vol. 195, 108953.
13. Nouri, A., Shirvan, A.R., Li, Y., Wen, C. Additive manufacturing of metallic and polymeric load-bearing biomaterials using laser powder bed fusion: A review, *Journal of Materials Science & Technology*, 2021: 94, 196-215.
14. Book Chapter
Sheet Lamination Processes
Gibson, I., Rosen, D., Stucker, B.
New York, NY: Springer New York
Additive Manufacturing Technologies, p. 219-244
15. Saboori, A., Gallo, D., Biamino, S., Fino, P., Lombardi, M. An Overview of Additive Manufacturing of Titanium Components by Directed Energy Deposition: Microstructure and Mechanical Properties, *Applied Science*, 2017: (7), 883.
16. Wu, H.C., Chen T.C. Quality control issues in 3D-printing manufacturing: a review, *Rapid Prototyping Journal*, 2018: 24 (3), 607-614.
17. Snow, Z., Diehl, B., Reutzel, E., Nassar, R. Toward in-situ flaw detection in laser powder bed fusion additive manufacturing through layerwise imagery and machine learning, *Journal of Manufacturing Systems*, 2021: 59, 12-26.
18. Book Chapter
Handbook of Nondestructive Evaluation, Second Edition
Hellier, C.J.
McGraw Hill, 2013
1.4. NONDESTRUCTIVE VERSUS DESTRUCTIVE TESTS
19. Charalampous, P., Kostavelis, I, Tzovaras, D. Non-destructive quality control methods in additive manufacturing: a survey, *Rapid Prototyping Journal*, 2020: 26, (4), 777-790.
20. Book Chapter
Handbook of Nondestructive Evaluation, Second Edition
Hellier, C.J.
McGraw Hill, 2013
1.1. WHAT IS NONDESTRUCTIVE TESTING?
21. Wang, B., Zhong, S., Lee, T.L., Non-destructive testing and evaluation of composite materials/structures: A state-of-the-art review, *Advances in Mechanical Engineering*, 2020: Vol. 12, (4), 1-28.
22. Balageas, D., Maldague, X., Burleigh, D., Vavilov, V.P., Oswald-Tranta, B., Roche, J.M., Pradere, C., Carlomagno, G.M. Thermal (IR) and Other NDT Techniques for Improved Material Inspection, *Journal of Nondestructive Evaluation*, 2016: 35:18 DOI 10.1007/s10921-015-0331-7.

23. Book Chapter
Practical Acoustic Emission Testing
The Japanese Society for Non-Destructive Inspection
Springer Japan, 2016
Principles of the Acoustic Emission (AE) Method and Signal Processing, p. 5-34.
24. Dunegan, H.L., Harris, D.O., Tatro, C.A. Fracture Analysis by Use of Acoustic Emission, *Engineering Fracture Mechanics*, 1968: 168, Vol. 1, p. 105-122.
25. Hamstad, M.A. A Review: Acoustic Emission, a Tool for Composite-Materials Studies. *Experimental Mechanics*, 1986: 26: 7-13.
26. Lozev, M.G., Clemena, G.G., Duke, J.C., Jr., Sison, M.F., Jr. and Horne, M.R. Acoustic Emission Monitoring of Steel Bridge Members, 1997: Virginia Transportation Research Council and Virginia Department of Transportation, Virginia, USA.
27. Sison, M., Duke, J.C., Jr., Lozev, M.G. and Clemena, G.G. "Analysis of acoustic emissions from a steel bridge hanger", *Research in Nondestructive Analysis*, 1998: Vol. 10, No. 3, pp. 123–145.
28. Gong, Z., Nyborg, E.O. and Oommen, G. "Acoustic emission monitoring of steel railroad bridges", *Materials Evaluation*, 1992: Vol. 50, No. 7, pp. 883–887.
29. Book Chapter
Handbook of Advanced Nondestructive Evaluation
Springer, 2019
Mayo, S., Endrizzi, M.
X-Ray Phase Contrast Methods, p. 1053-1093
30. Roentgen W. On a new kinds of rays, *Science*, 1896: 3 (59), 227–231.
31. Bonse, U., Hart, M. An x-ray interferometer, *Appl Phys Lett*, 1965: 6:155–156. <https://doi-org.proxy.library.vanderbilt.edu/10.1063/1.1754212>
32. Goetz, K., Kalashnikov. M.P., Mikhailov, Y.A., Sklizkov, G.V., Fedotov, S.I., Foerster, E, Zaumseil, P. Measurements of the parameters of shell targets for laser thermonuclear fusion using an x-ray Schlieren method, *Sov J Quantum Electron*, 1979: 9:607
33. Wagner. A, Sachse, A, Keller. M, Aurich, M., Wetzel, W.D., Hortschansky, P., Schmuck, K., Lohmann, M., Reime, B., Metge, J., Arfelli, F., Menk, R., Rigon, L., Muehleman, C., Bravin, A., Coan, P., Mollenhauer, J. Qualitative evaluation of titanium implant integration into bone by diffraction enhanced imaging, *Phys Med Biol*, 2006: 51:1313–1324.
34. Book Chapter
Handbook of Advanced Nondestructive Evaluation
Springer, 2019
Kastner, J., Heinzl, C.
X-Ray Tomography, p. 1095-1166

35. Vavilov, V.P., Burleigh, D.D. Review of pulsed thermal NDT: Physical principles, theory and data processing. *Nondestructive T&E International*, 2015: Vol. 73, 28-52. online. <https://doi-org.proxy.library.vanderbilt.edu/10.1016/j.ndteint.2015.03.003>

36. Parker, R.C., Marshal, P.R., The Measurement of the Temperature of Sliding Surfaces, with Particular Reference to Railway Brake Blocks, Research Article, First Published June 1, 1948. https://doi.org/10.1243/PIME_PROC_1948_158_026_02

37. Book Chapter
Handbook of Advanced Nondestructive Evaluation
Springer, 2019
Yang, L., Li, J.
Shearography, p. 383-419

38. Book Chapter
Handbook of Advanced Nondestructive Evaluation
Springer, 2019
Jonuscheit, J.
Terahertz Techniques in NDE, p. 967-985

39. Nash, Christopher John. Non-Destructive Evaluation for Mechanical Systems using Passive Thermal Methods. 31 Aug. 2020. Vanderbilt University.

40. Rahman, M., Schott, N.R., Sadhu, L.K., Glass Transition o ABS in 3D Printing, Excerpt from the Proceedings of the 2016 COMSOL Conference in Boston.

41. Li, S., Yu, X., Bao, H., Yang, N. High Thermal Conductivity of Bulk Epoxy Resin by Bottom-Up Parallel-Linking and Strain: A Molecular Dynamics Study, *Journal of Physical Chemistry*, 2018: 122, 24, 1,3140-1,3147.

42. Chung, S.L., Lin, J.S. Thermal Conductivity of Epoxy Resin Composites Filled with Combustion Synthesized h-BN Particles, *Molecules*, 2016: 21(5), 670.

43. Shimamura, A., Hotta, Y, Hyuga, H., Hotta, M, Hirao, K. Improving the thermal conductivity of epoxy composites using a combustion-synthesized aggregated β -Si₃N₄ filler with randomly oriented grains, *Scientific Reports*, 2020: 10, Article number: 14926.

44. Evseeva, L.E., Tanaeva, S.A. FEATURES OF THERMOPHYSICAL PROPERTIES OF MODIFIED EPOXY COMPOSITES AT LOW TEMPERATURES
[Features of thermophysical properties of modified epoxy \(escm.eu.org\)](http://escm.eu.org)

45. The Engineering Toolbox, Composite Resources [Polymers - Specific Heats \(engineeringtoolbox.com\)](http://engineeringtoolbox.com)

Appendices

Appendix A:

In Chapter 2, the FTCS equations are discussed. Schematics of the parts are shown below in Figure A.1, A.2, and A.3.

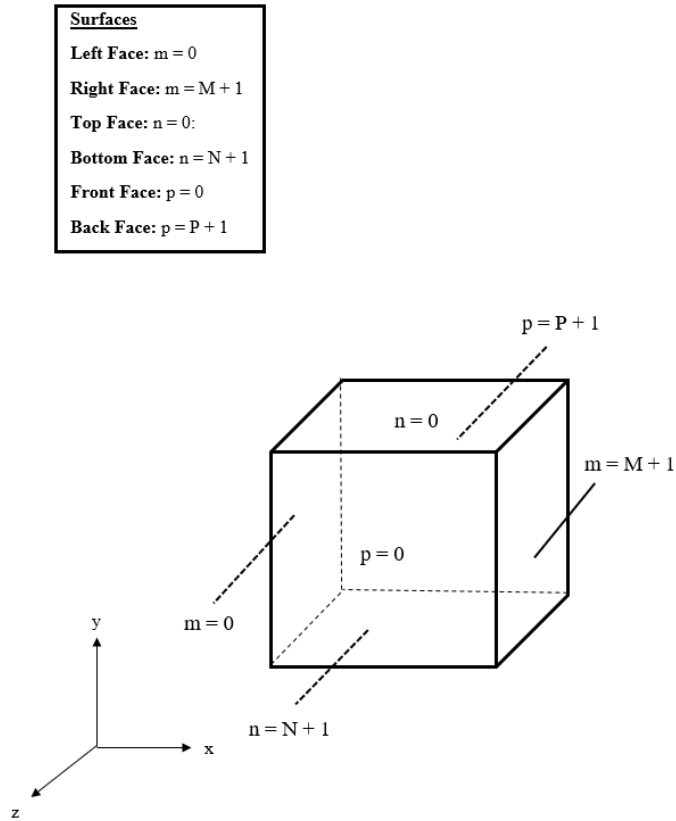


Figure A.1: Schematic of surface boundaries

Edges	
Top Left Edge:	$m = 0, n = 0$
Top Front Edge:	$n = 0, p = 0$
Left Back Edge:	$m = 0, p = P + 1$
Bottom Left Edge:	$m = 0, n = N + 1$
Top Back Edge:	$n = 0, p = P + 1$
Top Right Edge:	$m = M + 1, n = 0$
Right Back Edge:	$m = M + 1, p = P + 1$
Bottom Back Edge:	$n = N + 1, p = P + 1$
Right Front Edge:	$m = M + 1, p = 0$
Bottom Right Edge:	$m = M + 1, n = N + 1$
Bottom Front Edge:	$n = N + 1, p = 0$
Left Front Edge:	$m = 0, p = 0$

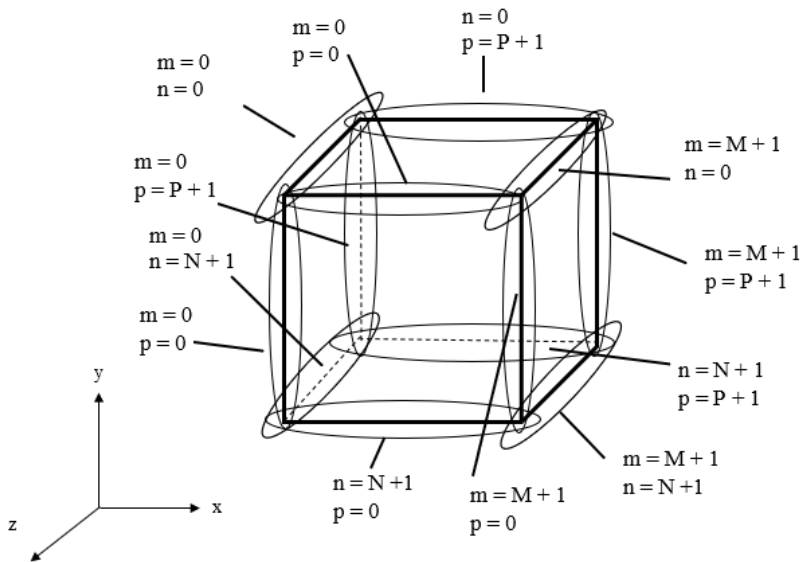


Figure A.2: Schematic of edge boundaries

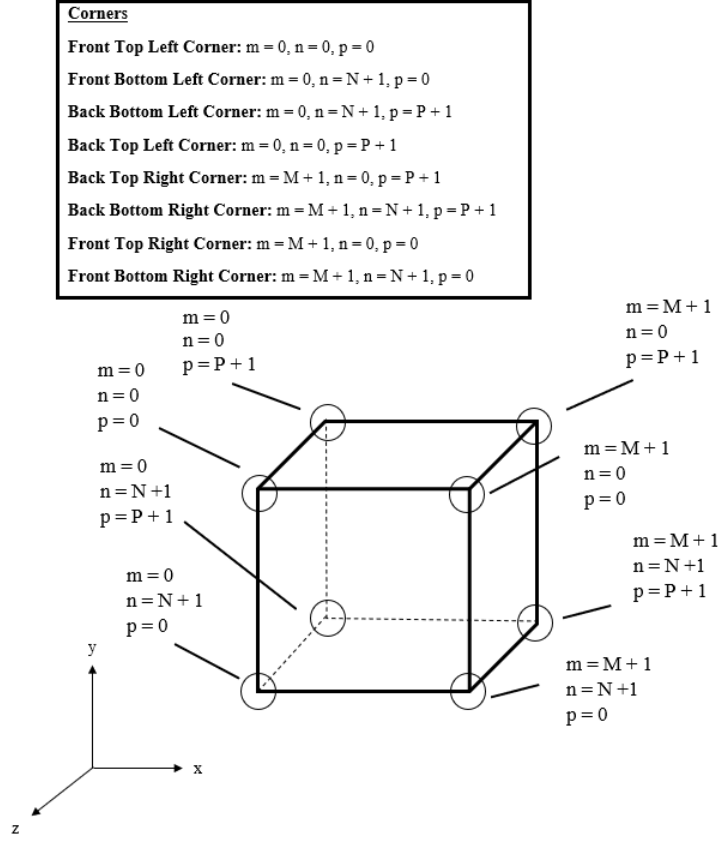


Figure A.3: Schematic of corner boundaries

The notation used in Figure A.1, A.2, and A.3 will be used in the FTCS equations. Let

$$r_x = \frac{k\Delta t}{\rho C_p \Delta x^2}; r_y = \frac{k\Delta t}{\rho C_p \Delta y^2}; r_z = \frac{k\Delta t}{\rho C_p \Delta z^2}.$$

All other variables are described in Chapter 2. The surface equations can be written as:

$$\text{Left Face [} m = 0 \text{]: } T_{m,n,p}^{i+1} = \left(1 - 2r_x - 2r_y - 2r_z - \frac{2r_x h \Delta x}{k_x}\right) T_{m,n,p}^i + 2r_x \left(T_{m+1,n,p}^i + \frac{h \Delta x}{k_x} T_\infty\right) + r_y (T_{m,n+1,p}^i + T_{m,n-1,p}^i) + r_z (T_{m,n,p+1}^i + T_{m,n,p-1}^i) \quad (\text{A.1})$$

$$\text{Right Face [} m = M + 1 \text{]: } T_{m,n,p}^{i+1} = \left(1 - 2r_x - 2r_y - 2r_z - \frac{2r_x h \Delta x}{k_x}\right) T_{m,n,p}^i + 2r_x \left(T_{m-1,n,p}^i + \frac{h \Delta x}{k_x} T_\infty\right) + r_y (T_{m,n+1,p}^i + T_{m,n-1,p}^i) + r_z (T_{m,n,p+1}^i + T_{m,n,p-1}^i) \quad (\text{A.2})$$

$$\text{Top Face [} n = 0 \text{]: } T_{m,n,p}^{i+1} = \left(1 - 2r_x - 2r_y - 2r_z - \frac{2r_y h \Delta y}{k_y}\right) T_{m,n,p}^i + r_x (T_{m+1,n,p}^i + T_{m-1,n,p}^i) + 2r_y \left(T_{m,n+1,p}^i + \frac{h \Delta y}{k_y} T_\infty\right) + r_z (T_{m,n,p+1}^i + T_{m,n,p-1}^i) \quad (\text{A.3})$$

$$\text{Bottom Face [n = N + 1]: } T_{m,n,p}^{i+1} = \left(1 - 2r_x - 2r_y - 2r_z - \frac{2r_y h \Delta y}{k_y}\right) T_{m,n,p}^i + r_x (T_{m+1,n,p}^i + T_{m-1,n,p}^i) + 2r_y \left(T_{m,n-1,p}^i + \frac{h \Delta y}{k_y} T_\infty\right) + r_z (T_{m,n,p+1}^i + T_{m,n,p-1}^i) \quad (\text{A. 4})$$

$$\text{Front Face [p = 0]: } T_{m,n,p}^{i+1} = \left(1 - 2r_x - 2r_y - 2r_z - \frac{2r_z h \Delta z}{k_z}\right) T_{m,n,p}^i + r_x (T_{m+1,n,p}^i + T_{m-1,n,p}^i) + r_y (T_{m,n+1,p}^i + T_{m,n-1,p}^i) + 2r_z \left(T_{m,n,p+1}^i + \frac{h \Delta z}{k_z} T_\infty\right) \quad (\text{A. 5})$$

$$\text{Back Face [p = P + 1]: } T_{m,n,p}^{i+1} = \left(1 - 2r_x - 2r_y - 2r_z - \frac{2r_z h \Delta z}{k_z}\right) T_{m,n,p}^i + r_x (T_{m+1,n,p}^i + T_{m-1,n,p}^i) + r_y (T_{m,n+1,p}^i + T_{m,n-1,p}^i) + 2r_z \left(T_{m,n,p-1}^i + \frac{h \Delta z}{k_z} T_\infty\right). \quad (\text{A. 6})$$

The edge equations can be written as:

$$\text{Top Left Edge [m = 0, n = 0]: } T_{m,n,p}^{i+1} = \left(1 - 2r_x - 2r_y - 2r_z - \frac{2r_x h \Delta x}{k_x} - \frac{2r_y h \Delta y}{k_y}\right) T_{m,n,p}^i + 2r_x \left(T_{m+1,n,p}^i + \frac{h \Delta x}{k_x} T_\infty\right) + 2r_y \left(T_{m,n+1,p}^i + \frac{h \Delta y}{k_y} T_\infty\right) + r_z (T_{m,n,p+1}^i + T_{m,n,p-1}^i) \quad (\text{A. 7})$$

$$\text{Bottom Left Edge [m = 0, n = N + 1]: } T_{m,n,p}^{i+1} = \left(1 - 2r_x - 2r_y - 2r_z - \frac{2r_x h \Delta x}{k_x} - \frac{2r_y h \Delta y}{k_y}\right) T_{m,n,p}^i + 2r_x \left(T_{m+1,n,p}^i + \frac{h \Delta x}{k_x} T_\infty\right) + 2r_y \left(T_{m,n-1,p}^i + \frac{h \Delta y}{k_y} T_\infty\right) + r_z (T_{m,n,p+1}^i + T_{m,n,p-1}^i) \quad (\text{A. 8})$$

$$\text{Top Right Edge [m = M + 1, n = 0]: } T_{m,n,p}^{i+1} = \left(1 - 2r_x - 2r_y - 2r_z - \frac{2r_x h \Delta x}{k_x} - \frac{2r_y h \Delta y}{k_y}\right) T_{m,n,p}^i + 2r_x \left(T_{m-1,n,p}^i + \frac{h \Delta x}{k_x} T_\infty\right) + 2r_y \left(T_{m,n+1,p}^i + \frac{h \Delta y}{k_y} T_\infty\right) + r_z (T_{m,n,p+1}^i + T_{m,n,p-1}^i) \quad (\text{A. 9})$$

$$\text{Bottom Right Edge [m = M + 1, n = N + 1]: } T_{m,n,p}^{i+1} = \left(1 - 2r_x - 2r_y - 2r_z - \frac{2r_x h \Delta x}{k_x} - \frac{2r_y h \Delta y}{k_y}\right) T_{m,n,p}^i + 2r_x \left(T_{m-1,n,p}^i + \frac{h \Delta x}{k_x} T_\infty\right) + 2r_y \left(T_{m,n-1,p}^i + \frac{h \Delta y}{k_y} T_\infty\right) + r_z (T_{m,n,p+1}^i + T_{m,n,p-1}^i) \quad (\text{A. 10})$$

$$\text{Left Front Edge [m = 0, p = 0]: } T_{m,n,p}^{i+1} = \left(1 - 2r_x - 2r_y - 2r_z - \frac{2r_x h \Delta x}{k_x} - \frac{2r_z h \Delta z}{k_z}\right) T_{m,n,p}^i + 2r_x \left(T_{m+1,n,p}^i + \frac{h \Delta x}{k_x} T_\infty\right) + r_y (T_{m,n+1,p}^i + T_{m,n-1,p}^i) + 2r_z \left(T_{m,n,p+1}^i + \frac{h \Delta z}{k_z} T_\infty\right) \quad (\text{A. 11})$$

$$\text{Left Back Edge [m = 0, p = P + 1]: } T_{m,n,p}^{i+1} = \left(1 - 2r_x - 2r_y - 2r_z - \frac{2r_x h \Delta x}{k_x} - \frac{2r_z h \Delta z}{k_z}\right) T_{m,n,p}^i + 2r_x \left(T_{m+1,n,p}^i + \frac{h \Delta x}{k_x} T_\infty\right) + r_y (T_{m,n+1,p}^i + T_{m,n-1,p}^i) + 2r_z \left(T_{m,n,p-1}^i + \frac{h \Delta z}{k_z} T_\infty\right) \quad (\text{A. 12})$$

$$\text{Right Front Edge [m = M + 1, p = 0]: } T_{m,n,p}^{i+1} = \left(1 - 2r_x - 2r_y - 2r_z - \frac{2r_x h \Delta x}{k_x} - \frac{2r_z h \Delta z}{k_z}\right) T_{m,n,p}^i + 2r_x \left(T_{m-1,n,p}^i + \frac{h \Delta x}{k_x} T_\infty\right) + r_y (T_{m,n+1,p}^i + T_{m,n-1,p}^i) + 2r_z \left(T_{m,n,p+1}^i + \frac{h \Delta z}{k_z} T_\infty\right) \quad (\text{A. 13})$$

$$\text{Right Back Edge [m = M + 1, p = P + 1]: } T_{m,n,p}^{i+1} = \left(1 - 2r_x - 2r_y - 2r_z - \frac{2r_x h \Delta x}{k_x} - \frac{2r_z h \Delta z}{k_z}\right) T_{m,n,p}^i + 2r_x \left(T_{m-1,n,p}^i + \frac{h \Delta x}{k_x} T_\infty\right) + r_y (T_{m,n+1,p}^i + T_{m,n-1,p}^i) + 2r_z \left(T_{m,n,p-1}^i + \frac{h \Delta z}{k_z} T_\infty\right) \quad (\text{A. 14})$$

$$\begin{aligned} \text{Top Front Edge [n = 0, p = 0]: } T_{m,n,p}^{i+1} = & \left(1 - 2r_x - 2r_y - 2r_z - \frac{2r_y h \Delta y}{k_y} - \frac{2r_z h \Delta z}{k_z}\right) T_{m,n,p}^i + \\ & r_x (T_{m+1,n,p}^i + T_{m-1,n,p}^i) + 2r_y \left(T_{m,n+1,p}^i + \frac{h \Delta y}{k_y} T_\infty\right) + 2r_z \left(T_{m,n,p+1}^i + \frac{h \Delta z}{k_z} T_\infty\right) \end{aligned} \quad (\text{A.15})$$

$$\begin{aligned} \text{Top Back Edge [n = 0, p = P + 1]: } T_{m,n,p}^{i+1} = & \left(1 - 2r_x - 2r_y - 2r_z - \frac{2r_y h \Delta y}{k_y} - \frac{2r_z h \Delta z}{k_z}\right) T_{m,n,p}^i + \\ & r_x (T_{m+1,n,p}^i + T_{m-1,n,p}^i) + 2r_y \left(T_{m,n+1,p}^i + \frac{h \Delta y}{k_y} T_\infty\right) + 2r_z \left(T_{m,n,p-1}^i + \frac{h \Delta z}{k_z} T_\infty\right) \end{aligned} \quad (\text{A.16})$$

$$\begin{aligned} \text{Bottom Front Edge [n = N + 1, p = 0]: } T_{m,n,p}^{i+1} = & \left(1 - 2r_x - 2r_y - 2r_z - \frac{2r_y h \Delta y}{k_y} - \frac{2r_z h \Delta z}{k_z}\right) T_{m,n,p}^i + \\ & r_x (T_{m+1,n,p}^i + T_{m-1,n,p}^i) + 2r_y \left(T_{m,n-1,p}^i + \frac{h \Delta y}{k_y} T_\infty\right) + 2r_z \left(T_{m,n,p+1}^i + \frac{h \Delta z}{k_z} T_\infty\right) \end{aligned} \quad (\text{A.17})$$

$$\begin{aligned} \text{Bottom Back Edge [n = N + 1, p = P + 1]: } T_{m,n,p}^{i+1} = & \left(1 - 2r_x - 2r_y - 2r_z - \frac{2r_y h \Delta y}{k_y} - \right. \\ & \left. \frac{2r_z h \Delta z}{k_z}\right) T_{m,n,p}^i + r_x (T_{m+1,n,p}^i + T_{m-1,n,p}^i) + 2r_y \left(T_{m,n-1,p}^i + \frac{h \Delta y}{k_y} T_\infty\right) + 2r_z \left(T_{m,n,p-1}^i + \right. \\ & \left. \frac{h \Delta z}{k_z} T_\infty\right) \end{aligned} \quad (\text{A.18})$$

The corner nodes can be written as:

$$\begin{aligned} \text{Front Top Left Corner [m = 0, n = 0, p = 0]: } T_{m,n,p}^{i+1} = & \left(1 - 2r_x - 2r_y - 2r_z - \frac{2r_x h \Delta x}{k_x} - \frac{2r_y h \Delta y}{k_y} - \right. \\ & \left. \frac{2r_z h \Delta z}{k_z}\right) T_{m,n,p}^i + 2r_x \left(T_{m+1,n,p}^i + \frac{h \Delta x}{k_x} T_\infty\right) + 2r_y \left(T_{m,n+1,p}^i + \frac{h \Delta y}{k_y} T_\infty\right) + 2r_z \left(T_{m,n,p+1}^i + \right. \\ & \left. \frac{h \Delta z}{k_z} T_\infty\right) \end{aligned} \quad (\text{A.19})$$

$$\begin{aligned} \text{Front Bottom Left Corner [m = 0, n = N + 1, p = 0]: } T_{m,n,p}^{i+1} = & \left(1 - 2r_x - 2r_y - 2r_z - \frac{2r_x h \Delta x}{k_x} - \right. \\ & \left. \frac{2r_y h \Delta y}{k_y} - \frac{2r_z h \Delta z}{k_z}\right) T_{m,n,p}^i + 2r_x \left(T_{m+1,n,p}^i + \frac{h \Delta x}{k_x} T_\infty\right) + 2r_y \left(T_{m,n-1,p}^i + \frac{h \Delta y}{k_y} T_\infty\right) + 2r_z \left(T_{m,n,p+1}^i + \right. \\ & \left. \frac{h \Delta z}{k_z} T_\infty\right) \end{aligned} \quad (\text{A.20})$$

$$\begin{aligned} \text{Back Top Left Corner [m = 0, n = 0, p = P + 1]: } T_{m,n,p}^{i+1} = & \left(1 - 2r_x - 2r_y - 2r_z - \frac{2r_x h \Delta x}{k_x} - \frac{2r_y h \Delta y}{k_y} - \right. \\ & \left. \frac{2r_z h \Delta z}{k_z}\right) T_{m,n,p}^i + 2r_x \left(T_{m-1,n,p}^i + \frac{h \Delta x}{k_x} T_\infty\right) + 2r_y \left(T_{m,n+1,p}^i + \frac{h \Delta y}{k_y} T_\infty\right) + 2r_z \left(T_{m,n,p-1}^i + \right. \\ & \left. \frac{h \Delta z}{k_z} T_\infty\right) \end{aligned} \quad (\text{A.21})$$

$$\begin{aligned} \text{Back Bottom Left Corner [m = 0, n = N + 1, p = P + 1]: } T_{m,n,p}^{i+1} = & \left(1 - 2r_x - 2r_y - 2r_z - \frac{2r_x h \Delta x}{k_x} - \right. \\ & \left. \frac{2r_y h \Delta y}{k_y} - \frac{2r_z h \Delta z}{k_z}\right) T_{m,n,p}^i + 2r_x \left(T_{m+1,n,p}^i + \frac{h \Delta x}{k_x} T_\infty\right) + 2r_y \left(T_{m,n-1,p}^i + \frac{h \Delta y}{k_y} T_\infty\right) + 2r_z \left(T_{m,n,p-1}^i + \right. \\ & \left. \frac{h \Delta z}{k_z} T_\infty\right) \end{aligned} \quad (\text{A.22})$$

$$\text{Front Top Right Corner [m = M + 1, n = 0, p = 0]: } T_{m,n,p}^{i+1} = \left(1 - 2r_x - 2r_y - 2r_z - \frac{2r_x h \Delta x}{k_x} - \frac{2r_y h \Delta y}{k_y} - \frac{2r_z h \Delta z}{k_z} \right) T_{m,n,p}^i + 2r_x \left(T_{m-1,n,p}^i + \frac{h \Delta x}{k_x} T_\infty \right) + 2r_y \left(T_{m,n+1,p}^i + \frac{h \Delta y}{k_y} T_\infty \right) + 2r_z \left(T_{m,n,p+1}^i + \frac{h \Delta z}{k_z} T_\infty \right) \quad (\text{A.23})$$

$$\text{Front Bottom Right Corner [m = M + 1, n = N + 1, p = 0]: } T_{m,n,p}^{i+1} = \left(1 - 2r_x - 2r_y - 2r_z - \frac{2r_x h \Delta x}{k_x} - \frac{2r_y h \Delta y}{k_y} - \frac{2r_z h \Delta z}{k_z} \right) T_{m,n,p}^i + 2r_x \left(T_{m-1,n,p}^i + \frac{h \Delta x}{k_x} T_\infty \right) + 2r_y \left(T_{m,n-1,p}^i + \frac{h \Delta y}{k_y} T_\infty \right) + 2r_z \left(T_{m,n,p+1}^i + \frac{h \Delta z}{k_z} T_\infty \right) \quad (\text{A.24})$$

$$\text{Back Top Right Corner [m = M + 1, n = 0, p = P + 1]: } T_{m,n,p}^{i+1} = \left(1 - 2r_x - 2r_y - 2r_z - \frac{2r_x h \Delta x}{k_x} - \frac{2r_y h \Delta y}{k_y} - \frac{2r_z h \Delta z}{k_z} \right) T_{m,n,p}^i + 2r_x \left(T_{m-1,n,p}^i + \frac{h \Delta x}{k_x} T_\infty \right) + 2r_y \left(T_{m,n+1,p}^i + \frac{h \Delta y}{k_y} T_\infty \right) + 2r_z \left(T_{m,n,p-1}^i + \frac{h \Delta z}{k_z} T_\infty \right) \quad (\text{A.25})$$

$$\text{Back Bottom Right Corner [m = M + 1, n = N + 1, p = P + 1]: } T_{m,n,p}^{i+1} = \left(1 - 2r_x - 2r_y - 2r_z - \frac{2r_x h \Delta x}{k_x} - \frac{2r_y h \Delta y}{k_y} - \frac{2r_z h \Delta z}{k_z} \right) T_{m,n,p}^i + 2r_x \left(T_{m-1,n,p}^i + \frac{h \Delta x}{k_x} T_\infty \right) + 2r_y \left(T_{m,n-1,p}^i + \frac{h \Delta y}{k_y} T_\infty \right) + 2r_z \left(T_{m,n,p-1}^i + \frac{h \Delta z}{k_z} T_\infty \right). \quad (\text{A.26})$$